Contemporary strain rates in the northern Basin and Range province from GPS data

R. A. Bennett

Harvard-Smithsonian Center for Astrophysics, Cambridge, Massachusetts, USA

B. P. Wernicke, N. A. Niemi,[1] and A. M. Friedrich[2]

Department of Geological and Planetary Sciences, California Institute of Technology, Pasadena, California, USA

J. L. Davis

Harvard-Smithsonian Center for Astrophysics, Cambridge, Massachusetts, USA

Received 5 November 2001; revised 29 August 2002; accepted 6 September 2002; published 21 March 2003.

[1] We investigate the distribution of active deformation in the northern Basin and Range province using data from continuous GPS (CGPS) networks, supplemented by additional campaign data from the Death Valley, northern Basin and Range, and Sierra Nevada–Great Valley regions. To understand the contemporary strain rate field in the context of the greater Pacific (P)–North America (NA) plate boundary zone, we use GPS velocities to estimate the average relative motions of the Colorado Plateau (CP), the Sierra Nevada–Great Valley (SNGV) microplate, and a narrow north-south elongate region in the central Great Basin (CGB) occupying the longitude band 114–117°W. We find that the SNGV microplate translates with respect to the CP at a rate of 11.4 ± 0.3 mm yr^{-1} oriented N47 ± 1°W and with respect to NA at a rate of ~12.4 mm yr^{-1} also oriented N47°W, slower than most previous geodetic estimates of SNGV-NA relative motion, and nearly 7° counterclockwise from the direction of P-NA relative plate motion. We estimate CGB-CP relative motion of 2.8 ± 0.2 mm yr^{-1} oriented N84 ± 5°W, consistent with roughly east-west extension within the eastern Great Basin (EGB). Velocity estimates from the EGB reveal diffuse extension across this region, with more rapid extension of 20 ± 1 nstr yr^{-1} concentrated in the eastern half of the region, which includes the Wasatch fault zone. We estimate SNGV-CGB relative motion of 9.3 ± 0.2 mm yr^{-1} oriented N37 ± 2°W, essentially parallel to P-NA relative plate motion. This rate is significantly slower than most previous geodetic estimates of deformation across the western Great Basin (WGB) but is generally consistent with paleoseismological inferences. The WGB region accommodates N37°W directed right lateral shear at rates of (1) 57 ± 9 nstr yr^{-1} across a zone of width ~125 km in the south (latitude ~36°N), (2) 25 ± 5 nstr yr^{-1} in the central region (latitude ~38°N), and (3) 36 ± 1 nstr yr^{-1} across a zone of width ~300 km in the north (latitude ~40°N). By construction there is no net extension or shortening perpendicular to SNGV-CGB relative motion. However, we observe about 8.6 ± 0.5 nstr yr^{-1} extension on average in the direction of shear from southeast to northwest within the Walker Lane belt, comparable to the average east-west extension rate of 10 ± 1 nstr yr^{-1} across the northern Basin and Range but implying a distinctly different mechanism of deformation from extension on north trending, range-bounding normal faults. An alternative model for this shear parallel deformation, in which extension is accommodated across a narrow, more rapidly extending zone that coincides with the central Nevada seismic belt, fits the WGB data slightly better. Local anomalies with respect to this simple kinematic model may reveal second-order deformation signals related to more local crustal dynamic phenomena, but significant improvements in velocity field resolution will be necessary to reveal this second-order pattern. *INDEX TERMS:* 1206 Geodesy and Gravity: Crustal movements—interplate (8155); 1208 Geodesy and Gravity: Crustal movements—intraplate (8110); 8107 Tectonophysics: Continental neotectonics; 8109 Tectonophysics: Continental tectonics—extensional (0905); *KEYWORDS:* GPS, crustal deformation, strain rates, Basin and Range. **Citation:** Bennett, R. A., B. P. Wernicke, N. A. Niemi, A. M. Friedrich, and J. L. Davis, Contemporary strain rates in the northern Basin and Range province from GPS data, *Tectonics*, *22*(2), 1008, doi:10.1029/2001TC001355, 2003.

1. Introduction

[2] Where plate boundary zones involve continental lithosphere, deformation of the continental plate tends to

[1]Now at Geological Science Department, University of Santa Barbara, Santa Barbara, California, USA.

[2]Now at Institut für Geowissenschaften, Universität Potsdam, Golm, Germany.

0278-7407/03/2001TC001355

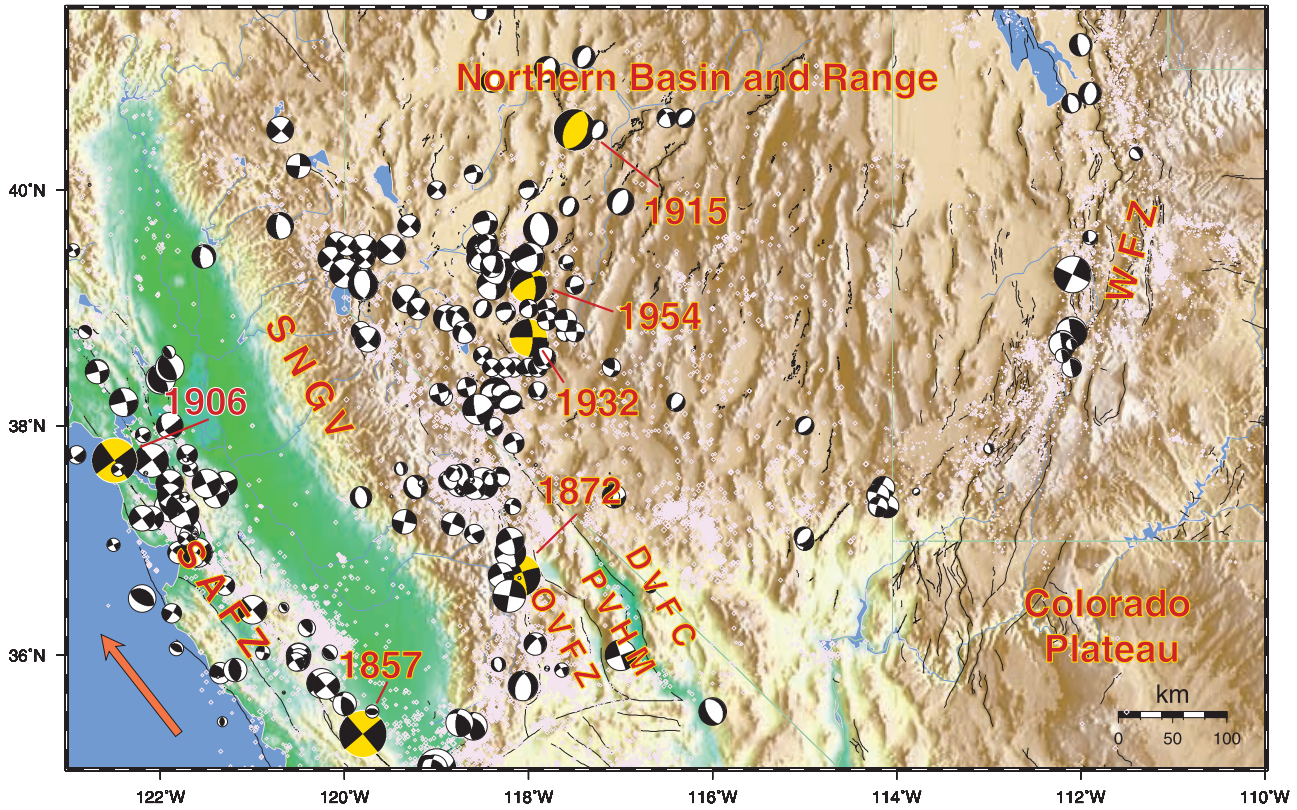

Figure 1a. Relief map of the northern Basin and Range province showing selected Quaternary faults (broken black lines), seismicity from southern and northern California earthquake centers, University of Nevada, Reno, and University of Utah catalogs (pink diamonds), earthquake focal mechanisms from *Shen-Tu et al.* [1998], and some of the major fault zones of the Pacific–North America plate boundary. Black quadrants of the focal mechanisms show compression first. Several important $M > 7$ events are labeled with their dates of occurrence. These are the 1857 Fort Tejon, 1872 Owens Valley, 1915 Pleasant Valley, 1932 Cedar Mountain, and 1954 Rainbow Mountain–Fairview Peak–Dixie Valley events. The red arrow in the Pacific Ocean shows the direction of Pacific plate motion with respect to North America. The Sierra Nevada–Great Valley microplate also translates with respect to North America. This motion is accommodated, in part, by strike-slip on the Owens Valley (OWFZ), Panamint Valley–Hunter Mountain (PVHM), and Death Valley–Furnace Creek (DVFC) fault zones. A key question is whether all of the deformation within the northern Basin and Range province is driven entirely by Pacific–North America relative plate motion, or whether other forces also play an important role within the interior deformation zone.

be diffusely accommodated on fault systems hundreds to thousands of kilometers wide [*Molnar and Tapponier*, 1975; *Thatcher*, 1995]. It is generally recognized that the width of these zones, in contrast to the narrow zones that characterize plate boundaries within oceanic lithosphere, is the result of the relative weakness of continental lithosphere [*England and McKenzie*, 1982]. Less clear, however, is the origin of forces driving deformation in continental plate boundary zones, in particular, the relative importance of stresses applied at the base or sides of the plates versus the stresses originating from gravitational potential gradients within the plates themselves [*Molnar*, 1988; *Wernicke*, 1992; *Sonder and Jones*, 1999]. The primary observable for testing dynamic models of plate boundary deformation is the large-scale, instantaneous velocity field of Earth's surface [e.g., *Flesch et al.*, 2000] because stresses and rheologies, while they may be estimated, are highly uncertain in comparison with direct kinematic measurements. This latter point has become especially true with the advent of space geodesy, which permits crustal velocity fields to be determined in a single self-consistent reference frame across the entire width of intracontinental deformation zones [e.g., *Bennett et al.*, 1999, 2002; *McClusky et al.*, 2000].

[3] One of the most striking examples of a diffuse plate boundary fault system is the Basin and Range province of the western United States (Figure 1a), which currently accommodates some 25% of the total strain budget between the Pacific and North America plates [*Minster and Jordan*, 1987; *Dixon et al.*, 1995; *Bennett et al.*, 1999]. The region lies east of the greater San Andreas fault zone, which slips an estimated ~39 mm yr^{-1} [*Freymueller et al.*, 1999; *Prescott et al.*, 2001], and the Sierra Nevada–Great Valley

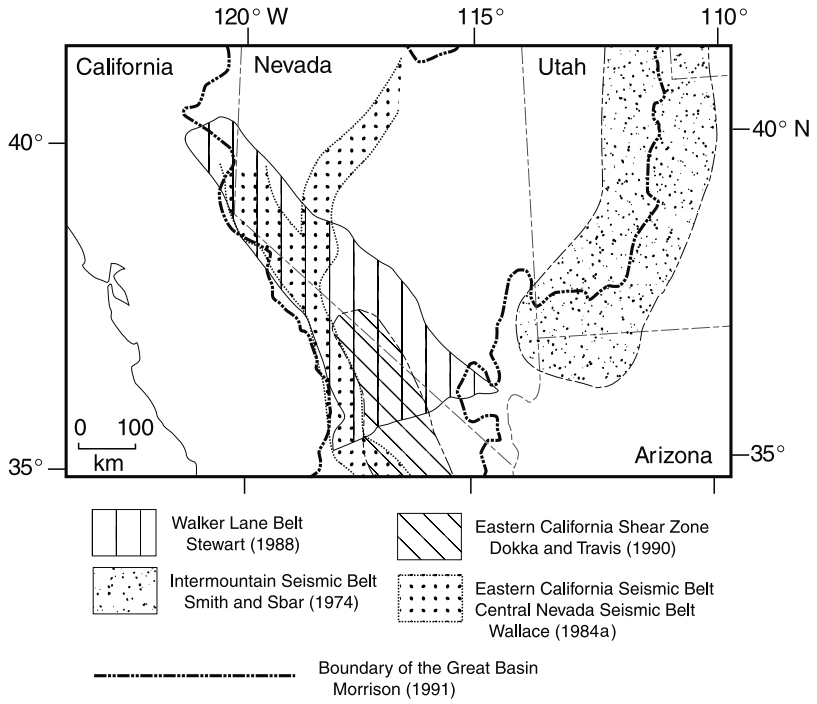

Figure 1b. Various tectonic elements of the northern Basin and Range province from the literature based on seismicity and geological patterns.

microplate, which moves northwest with rate estimates in the range of ~12–14 mm yr^{-1} relative to the continental interior [e.g., *Dixon et al.*, 2000]. It is generally agreed that the motion of this microplate results at least in part from shear applied by the Pacific plate and that some of the Pacific–North America relative plate motion is shunted toward the interior of the Cordillera east of the Sierra Nevada–Great Valley microplate via fault zones comprising the eastern California shear zone (ECSZ) such as the Owens Valley (OVFZ), the Panamint Valley–Hunter Mountain (PVHM), and the Death Valley–Furnace Creek (DVFC) (Figure 1a).

[4] Within this interior zone most of the deformation is accommodated within the Basin and Range physiographic province, which contains a broadly distributed system of Quaternary normal and strike-slip fault zones and relatively discrete belts of seismicity (Figure 1b). Four tectonic elements, which have been interpreted as components of the plate boundary deformation zone, have been defined within the province. Two of these elements have been defined on the basis of historical seismicity and include the eastern California/central Nevada seismic belt [*Wallace*, 1984a] and the Intermountain seismic belt [*Smith and Sbar*, 1974], which are localized on or near the eastern and western boundaries of the Basin and Range, respectively. Focal mechanisms for the eastern California/central Nevada seismic belt are predominantly right lateral strike-slip or normal, whereas those in the Intermountain seismic belt are predominantly normal (Figure 1a). The other two elements, which cover a wider region than the seismic belts, are defined on the basis of geological patterns. In the north the Walker Lane belt is defined primarily on the basis of physiography, where mountain ranges of diverse orientations within the belt contrast markedly with the generally north-northeast trending ranges to the east (Figure 1a). This relatively complex physiographic region contains domains of right and left lateral strike-slip faulting and normal faulting, generally interpreted as accommodating a substantial component of Pacific–North America relative plate motion via right shear and extension from mid-Miocene to recent time [e.g., *Wernicke et al.*, 1988]. In the south the ECSZ, which partly overlaps with the Walker Lane belt, is defined on the basis of a similarly complex system of late Miocene and younger right and left lateral strike-slip faults, also interpreted to have accommodated significant right shear since ~10 Ma (Figure 1b) [*Dokka and Travis*, 1990].

[5] Although the northern Basin and Range is generally regarded as an archetypal example of intracontinental extension [*Stewart*, 1971], it has become increasingly apparent that distributed right lateral shear is an important, if not dominant, component of the Quaternary strain rate field. A key question is whether all of the deformation accommodated in the Basin and Range results from horizontal tractions applied along the edge of North America, or whether other forces, such as basal tractions arising from asthenospheric upwelling or convective instabilities [*Parsons et al.*, 1994; *Humphreys*, 1995] or body forces arising from gravitational potential gradients [*Jones et al.*, 1996], play a major role within the interior deformation zone. If the whole of Basin and Range deformation can be ascribed to a system of right lateral shear, then the validity of models favoring forces other than plate boundary traction would be questionable. On the other hand, if the regional strain field contains patterns not easily modeled as a result of

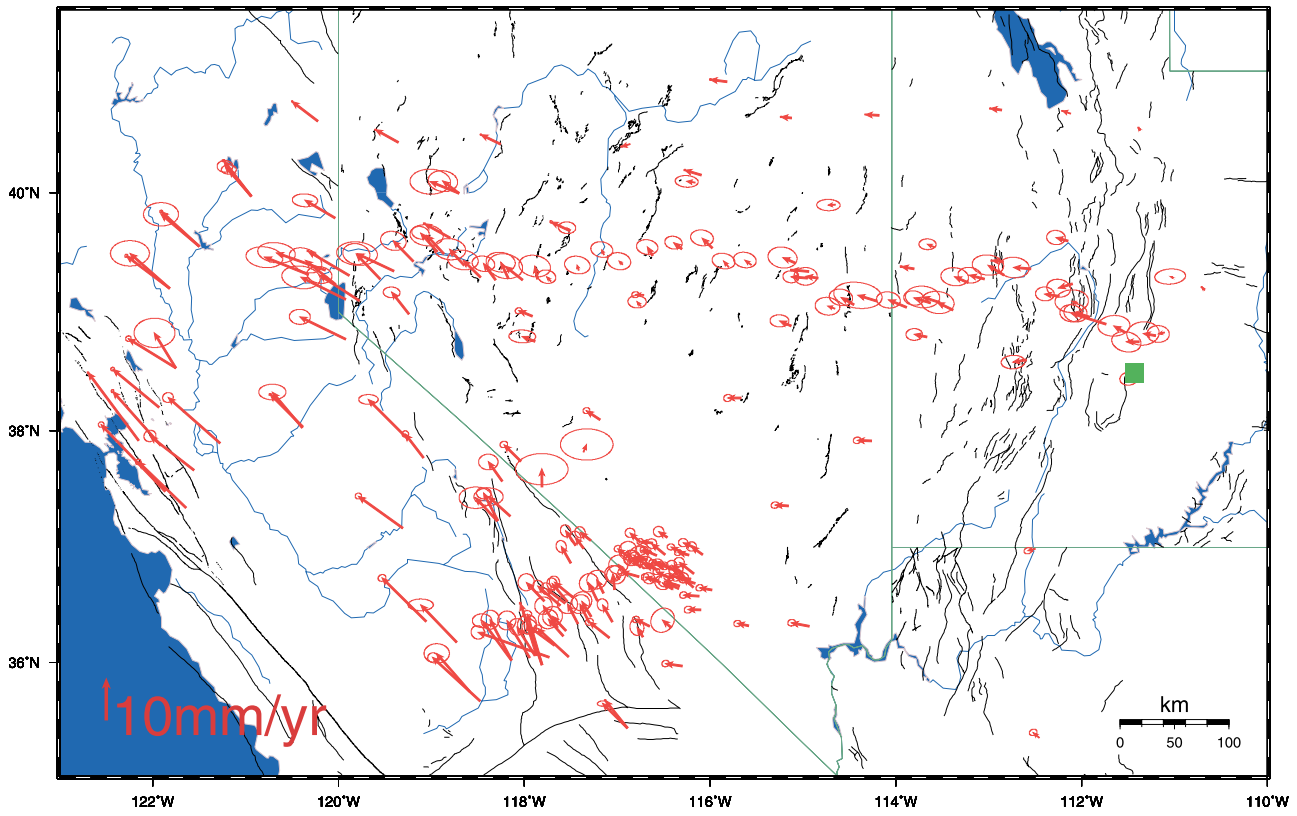

Figure 2. GPS velocities of sites in the Sierra Nevada–Great Valley microplate, northern Basin and Range, and Colorado Plateau regions with respect to North America. Error ellipses represent the 95% confidence level. Deformation is evident as far east as the WFZ (Figure 1a). Also shown are selected Quaternary faults (broken black lines). The green square shows the average geographic location of sites on the Colorado Plateau and represents the origin of the horizontal axes in Figure 4.

right lateral shear, alternative mechanisms will need to be explored. In this paper, we attempt to shed light on these issues using a dense set of high-precision horizontal velocity estimates for sites in and around the northern Basin and Range province. The primary data for this study are horizontal velocity estimates derived from continuous GPS (CGPS) data from the Basin and Range Geodetic Network (BARGEN) [*Bennett et al.*, 1998; *Wernicke et al.*, 2000]. We also use additional data from the Bay Area Regional Deformation (BARD) [*King et al.*, 1995; *Prescott et al.*, 2001] and International GPS Service (IGS) [*Beutler et al.*, 1994] CGPS networks and various campaign GPS data for networks in and around the northern Basin and Range [*Bennett et al.*, 1997; *Thatcher et al.*, 1999; *Dixon et al.*, 2000; *Gan et al.*, 2000], for a total of 211 velocity estimates.

2. Data

[6] Figure 2 shows the horizontal velocity estimates that comprise the primary data for this study. These estimates are also listed in Table 1. They were obtained from the BARGEN, BARD, IGS, and other networks. In this section we describe the data reductions leading to the site velocity estimates and briefly discuss (1) the issue of reference frame definition, (2) the methods that we adopted to aggregate the various campaign and CGPS data sets, and (3) the nature of the uncertainties that we adopted for the velocity estimates. We also qualitatively describe the velocity estimates, including an heuristic assessment of their resolving power. More quantitative analyses of the large-scale kinematics of the plate boundary zone and of the northern Basin and Range strain rate field are presented in following sections. We reserve analysis of the complex issue of vertical motion for future work. Horizontal motion is implied therefore throughout the remainder of this paper in all references to site motion and crustal deformation.

2.1. GPS Data Reduction

[7] We used the GAMIT software [*King and Bock*, 1999] to analyze phase data from the BARGEN CGPS network collected between epochs 1996.6 and 2001.3. We also incorporated into our analyses data from several other CGPS networks, including the BARD and IGS networks, using Receiver Independent Exchange (RINEX) data files downloaded from the University NAVSTAR Consortium (UNAVCO) and Scrips Orbit and Permanent Array Center (SOPAC) facilities and Software Independent Exchange (SINEX) data files downloaded from the SOPAC facility. Not all of the velocities for CGPS stations in Table 1 and Figure 2 represent data for this entire period of time, and

Table 1. Velocity Estimates Relative to North America[a]

Station[b] ID	Longitude, deg	Latitude, deg	Estimate		Uncertainty		Correlation Coefficient	Region[c]
			East	North	East	North		
67TJYUCC	243.604	36.813	−2.24	0.81	0.40	0.39	0.0193	CGB[d]
A187ECSZ	241.864	36.023	−5.39	10.11	0.93	0.97	0.0200	SNGV
A1ZZNBAR	239.961	39.791	−7.52	4.45	1.30	0.66	−0.0800	NWGB[d]
A21ZNBAR	239.858	39.358	−12.25	4.33	1.93	1.05	−0.1700	NWGB
A22ZNBAR	239.967	39.239	−7.52	6.00	1.67	1.29	−0.3300	NWGB
A23ZNBAR	240.077	39.111	−11.21	5.56	1.97	1.17	−0.1400	NWGB
A25ZNBAR	240.226	39.102	−10.05	6.45	1.29	0.87	−0.1400	NWGB
A27ZNBAR	240.450	39.283	−6.01	6.28	1.39	1.07	−0.1200	NWGB[d]
A28ZNBAR	240.595	39.350	−9.23	4.36	2.09	1.21	−0.1000	NWGB[d]
A29ZNBAR	240.807	39.429	−5.05	5.18	1.31	0.98	−0.1500	NWGB[d]
A2ZZNBAR	239.675	39.318	−11.02	4.41	1.89	1.07	−0.1400	NWGB
A3DDECSZ	242.576	36.340	−2.57	4.91	1.03	0.97	0.0000	SWGB
A3ZZNBAR	240.076	38.778	−11.48	5.59	1.08	0.77	−0.0200	NWGB
A7TJECSZ	243.604	36.813	−3.90	1.28	0.56	0.53	−0.0600	CGB[d]
A813ECSZ	242.325	36.150	−6.31	4.65	0.76	0.77	−0.0200	SWGB
AGUEYUCC	242.947	36.357	−2.42	4.22	0.55	0.62	−0.0841	SWGB
ALAMCGPS	244.842	37.358	−3.33	0.21	0.40	0.33	0.1124	CGB
APDIECSZ	243.837	36.690	−3.01	0.87	0.39	0.31	−0.0500	CGB[d]
APEXCGPS	245.068	36.319	−4.43	0.84	0.39	0.34	0.0984	CGB
ARGUCGPS	242.478	36.050	−7.81	7.18	0.39	0.34	0.0940	SWGB
BIZZNBAR	241.297	39.996	−4.03	3.06	1.51	1.07	−0.1000	NWGB
B21ZNBAR	241.133	39.494	−4.30	4.64	1.70	1.08	−0.1000	NWGB[d]
B22ZNBAR	241.354	39.398	−3.64	4.02	1.63	1.09	−0.1000	NWGB[d]
B23ZNBAR	241.528	39.299	−4.38	4.29	1.56	1.01	−0.1200	NWGB[d]
B25ZNBAR	241.689	39.274	−3.00	4.10	1.16	0.79	−0.1300	NWGB[d]
B27ZNBAR	241.827	39.286	−1.90	4.12	1.50	1.02	−0.1100	NWGB
B28ZNBAR	241.983	39.275	−4.39	3.44	1.78	1.28	−0.1400	NWGB
B29ZNBAR	242.141	39.284	−0.67	3.21	1.62	1.11	−0.1500	NWGB
B2ZZNBAR	241.061	39.513	−4.17	4.69	0.89	0.65	−0.1500	NWGB[d]
B3ZZNBAR	240.756	38.988	−4.29	5.47	0.86	0.55	−0.0500	NWGB[d]
BAREECSZ	243.325	36.843	−3.10	2.18	0.54	0.51	−0.0400	CGB[d]
BEATCGPS	243.379	37.040	−3.09	0.36	0.32	0.29	0.0989	CGB[d]
BL91ECSZ	243.425	36.809	−2.53	1.79	0.64	0.62	−0.1000	CGB[d]
BM25ECSZ	242.056	36.045	−5.69	9.30	0.93	0.97	0.0300	SWGB
BM8ZECSZ	243.022	36.724	−0.79	1.16	0.96	0.94	0.0200	SWGB
BRIBCGPS	237.847	37.919	−12.66	17.03	0.09	0.09	−0.0183	–
BRICECSZ	243.365	36.959	−2.66	0.49	0.54	0.51	−0.0200	CGB[d]
BULLCGPS	243.128	36.918	−2.85	2.10	0.36	0.33	0.1005	CGB[d]
BUSTCGPS	243.549	36.745	−2.96	1.34	0.35	0.31	0.0999	CGB[d]
C1ZZNBAR	242.491	39.686	−0.70	0.74	0.89	0.60	−0.0500	NWGB
C22ZNBAR	242.588	39.358	−0.40	1.25	1.31	0.91	−0.1300	NWGB
C24ZNBAR	242.858	39.487	−0.54	1.25	1.13	0.80	−0.1400	NWGB
C26ZNBAR	243.058	39.403	−0.89	0.86	1.20	0.88	−0.1200	NWGB
C28ZNBAR	243.379	39.477	−1.31	2.18	1.10	0.76	−0.1200	CGB
C2ZZNBAR	242.288	39.264	−1.08	1.14	0.93	0.69	−0.1400	NWGB
C3ZZNBAR	242.116	38.760	−3.21	1.22	1.37	0.66	−0.0500	CWGB[d]
CAN5ECSZ	243.822	36.776	−3.61	2.84	0.52	0.48	0.0000	CGB[d]
CASTCGPS	249.323	39.191	−0.67	0.67	0.07	0.06	0.0302	CP
CEDACGPS	247.140	40.681	−2.87	0.39	0.06	0.06	0.0243	EGB
CEDASNGV	241.410	35.750	−8.23	9.47	1.30	1.00	0.0000	SNGV[e,f]
CERRECSZ	242.213	36.538	−4.49	4.68	0.83	0.87	0.0200	SWGB
CHLOCGPS	243.234	36.747	−4.32	1.21	0.40	0.36	0.1162	SWGB[d]
CLAIYUCC	243.319	36.889	−3.81	0.57	0.82	0.77	0.0767	CGB[d]
CLAIECSZ	243.319	36.889	−2.09	1.11	0.94	0.98	0.0100	CGB[d]
CMBBCGPS	239.614	38.034	−8.15	8.16	0.12	0.11	0.0073	SNGV[e,f]
CMBBSNGV	239.610	38.030	−7.51	8.89	1.40	0.80	0.0000	SNGV[e,f]
CNDRCGPS	238.722	37.896	−13.02	11.47	0.55	0.50	0.0740	SNGV
COONCGPS	247.879	40.653	−2.02	0.67	0.07	0.06	0.0324	EGB
COSOCGPS	242.191	35.982	−5.45	15.41	0.10	0.09	−0.0198	–
COSOECSZ	242.191	35.982	−3.69	12.74	0.44	0.35	−0.0300	–
CRATCGPS	243.431	36.808	−3.19	0.97	0.29	0.27	0.0586	CGB[d]
D1ZZNBAR	243.839	40.084	−2.11	0.32	1.18	0.60	−0.0900	CGB
D22ZNBAR	244.024	39.543	−2.58	2.51	1.17	0.81	−0.1200	CGB
D24ZNBAR	244.201	39.381	−1.30	1.56	1.17	0.80	−0.1600	CGB
D26ZNBAR	244.444	39.402	−1.61	1.19	1.16	0.80	−0.1400	CGB
D28ZNBAR	244.918	39.416	−3.21	1.39	1.49	1.08	−0.1100	CGB
D2ZZNBAR	243.694	39.534	−2.04	1.57	0.89	0.66	−0.1300	CGB

Table 1. (continued)

Station[b] ID	Longitude, deg	Latitude, deg	Estimate		Uncertainty		Correlation Coefficient	Region[c]
			East	North	East	North		
D3ZZNBAR	243.254	39.056	−0.92	1.09	0.94	0.64	−0.0400	CWGB
DANTYUCC	243.274	36.226	−1.43	2.38	0.72	0.84	−0.0761	SWGB
DIABCGPS	238.084	37.879	12.05	13.58	0.14	0.15	−0.0154	–
DYERCGPS	241.961	37.743	−4.22	4.16	0.39	0.33	0.1074	CWGB[d]
E1ZZNBAR	245.348	39.902	−1.72	−0.10	1.20	0.58	−0.0300	CGB
E22ZNBAR	245.342	39.033	−1.81	0.65	1.27	0.91	−0.0900	CGB
E24ZNBAR	245.547	39.069	−3.22	1.81	1.20	0.85	−0.1300	CGB
E259NBAR	245.761	39.098	2.08	−4.69	7.37	4.43	−0.0900	–
E26ZNBAR	245.796	39.097	−4.77	1.47	2.48	1.35	−0.1700	CGB
E28ZNBAR	246.113	39.045	−4.50	1.87	1.22	0.83	−0.1000	CGB
E2ZZNBAR	245.047	39.290	−4.13	0.32	0.82	0.61	−0.0700	CGB
E3ZZNBAR	244.870	38.890	−2.87	1.25	0.97	0.62	−0.0300	CGB
ECHOCGPS	245.736	37.916	−3.56	0.12	0.40	0.33	0.1137	CGB
EGANCGPS	245.061	39.345	−4.31	0.40	0.10	0.09	0.0029	CGB
ELKOCGPS	244.183	40.915	−4.14	0.52	0.09	0.08	0.0010	CGB
ELYASNGV	245.160	39.290	−3.07	0.45	1.20	0.90	0.0000	CGB
FIZZNBAR	246.415	39.549	−1.72	0.72	0.88	0.55	−0.0200	EGB
F21ZNBAR	246.470	39.087	−4.26	1.36	1.76	1.11	−0.0600	EGB
F22ZNBAR	246.615	39.024	−3.86	1.86	1.69	1.14	−0.1000	EGB
F23XECSZ	243.138	36.858	−0.52	3.34	0.91	0.95	0.0200	CGB[d]
F23ZNBAR	246.776	39.254	−3.32	1.43	1.42	0.93	−0.1000	EGB
F25ZNBAR	246.954	39.283	−3.72	0.95	1.19	0.80	−0.1000	EGB
F27ZNBAR	247.163	39.317	−4.01	2.47	1.61	1.04	−0.0900	EGB
F28ZNBAR	247.454	39.367	−4.29	0.34	1.58	1.06	−0.0500	EGB
F2ZZNBAR	246.370	39.082	−4.11	1.24	1.03	0.74	−0.1000	EGB
F3ZZNBAR	246.333	38.795	−3.14	0.66	0.85	0.60	0.0000	EGB
FERNCGPS	247.545	35.342	−1.53	1.28	0.40	0.33	0.1309	CP
FLATYUCC	242.439	36.519	−4.72	3.63	0.52	0.60	−0.0962	SWGB
FOOTCGPS	246.195	39.369	−3.22	0.54	0.10	0.10	0.0220	EGB
FORKECSZ	242.116	36.062	−4.53	7.19	0.81	0.85	−0.0500	SWGB
FREDCGPS	247.501	36.988	−1.87	−0.47	0.39	0.32	0.1298	CP
G165ECSZ	242.788	36.542	−2.18	4.44	0.97	0.94	0.0900	SWGB
G1ZZNBAR	247.852	39.601	−2.99	0.84	0.96	0.73	−0.0500	EGB
G21ZNBAR	247.902	39.241	−3.48	−1.05	1.22	0.92	−0.1000	EGB
G22ZNBAR	247.958	39.079	−1.50	0.54	1.71	1.16	0.0400	EGB
G23ZNBAR	248.085	38.962	−3.51	1.11	1.19	0.93	−0.0900	EGB
G25ZNBAR	248.262	38.905	−8.72	2.70	1.16	0.87	−0.0800	–
G27ZNBAR	248.463	38.839	−2.67	1.53	1.64	1.06	0.0400	CP
G28ZNBAR	248.619	38.755	−3.20	0.01	1.50	1.05	−0.1700	CP
G29ZNBAR	248.794	38.808	−3.10	0.52	1.66	1.20	0.0600	CP
G2ZZNBAR	247.758	39.140	−3.58	0.53	0.96	0.71	−0.0400	EGB
G3ZZNBAR	247.406	38.603	−3.36	−0.55	1.22	0.69	0.0600	EGB
GABBCGPS	242.084	38.970	−3.39	1.39	0.35	0.31	0.0897	CWGB[d]
GARLCGPS	240.645	40.417	−5.72	3.18	0.07	0.06	−0.0011	NWGB[d]
GFLDSNGV	242.640	37.820	0.76	1.90	2.70	1.60	0.0000	CWGB[d]
GOLDCGPS	243.111	35.425	5.59	6.97	0.08	0.08	−0.0435	SWGB
GOLDECSZ	243.111	35.425	−6.22	6.18	0.55	0.27	0.1000	SWGB
GOO5ECSZ	242.265	36.047	−17.85	6.24	0.69	0.69	−0.0600	–
GOSHCGPS	245.820	40.640	−3.45	0.18	0.07	0.06	0.0216	CGB
GRAPYUCC	242.640	36.992	−2.08	2.79	0.56	0.63	−0.1263	SWGB
H1ZZNBAR	248.980	39.294	−0.62	0.28	1.58	0.78	0.1000	CP
H2ZZNBAR	248.889	38.833	−1.49	−0.35	1.14	0.86	−0.0200	CP
H3ZZNBAR	248.641	38.483	−3.10	−1.15	0.92	0.67	0.0800	CP
HEBECGPS	248.627	40.514	−0.35	0.70	0.07	0.06	0.0440	CP
HOLDECSZ	242.973	36.638	−0.40	3.97	0.86	0.82	0.0500	SWGB
HUNTYUCC	242.521	36.572	−4.58	3.76	0.53	0.61	−0.0882	SWGB
ISLKCGPS	241.526	35.662	−11.97	10.99	0.51	0.47	0.0834	SNGV[f]
JACKYUCC	242.460	36.532	−3.76	4.46	0.53	0.60	−0.0855	SWGB
JCTNECSZ	243.583	36.304	2.19	1.89	1.21	1.24	0.1300	SWGB
JNPRCGPS	240.915	37.772	−4.57	5.95	0.34	0.32	0.0039	CWGB
JOHNCGPS	243.901	36.459	−3.20	0.08	0.40	0.36	0.1066	CGB[d]
KMEDSNGV	241.860	36.020	−7.33	9.96	1.00	0.70	0.0000	SNGV[f]
L166ECSZ	242.450	36.279	−3.39	3.61	1.02	1.00	0.0600	SWGB
LEEFYUCC	242.388	36.497	−5.58	4.85	0.54	0.61	−0.0899	SWGB
LEWICGPS	243.138	40.404	−2.08	−0.65	0.09	0.08	0.0080	NWGB
LINDCGPS	240.942	36.360	−11.04	10.90	0.41	0.35	0.1057	SNGV[e,f]
LITTCGPS	243.692	36.746	−3.54	0.04	0.35	0.32	0.0978	CGB

Table 1. (continued)

Station[b] ID	Longitude, deg	Latitude, deg	Estimate		Uncertainty		Correlation Coefficient	Region[c]
			East	North	East	North		
M137ECSZ	242.700	36.349	−2.33	4.64	0.98	0.97	0.1200	SWGB
MERCCGPS	244.021	36.633	−3.12	0.54	0.37	0.33	0.1032	CGB[d]
MHCBCGPS	238.357	37.342	−11.98	11.54	0.29	0.28	0.0337	–
MILEECSZ	243.531	36.838	−3.43	0.99	0.39	0.31	−0.0400	CGB[d]
MINECGPS	243.904	40.148	−4.12	1.22	0.08	0.08	−0.0178	CGB
MN71ECSZ	243.851	36.994	−3.29	1.40	0.48	0.42	−0.0100	CGB[d]
MO93ECSZ	243.071	36.792	−1.36	1.76	0.99	0.97	0.0500	SWGB[d]
MONBCGPS	238.133	37.485	−16.05	16.72	0.29	0.28	0.0328	–
MONICGPS	243.284	39.148	−2.04	0.10	0.37	0.31	0.0883	CWGB
MUSBCGPS	240.691	37.170	−11.14	7.98	0.33	0.30	0.0274	SNGV[e,f,g]
NEV1YUCC	242.714	37.061	−2.65	2.06	0.53	0.57	−0.0808	SWGB
NEWPCGPS	242.491	39.686	−4.69	2.20	0.13	0.14	−0.0723	NWGB
OASISNGV	242.190	37.520	−0.04	4.50	2.70	1.60	0.0000	CWGB[d]
ORVBCGPS	238.500	39.555	−9.51	8.73	0.15	0.15	0.0046	SNGV[e,g]
ORVBSNGV	238.500	39.555	−9.58	8.06	1.80	1.20	0.0000	SNGV[e,g]
OVROECSZ	241.716	37.232	−3.53	6.87	0.75	0.58	−0.0300	CWGB
OVROSNGV	241.710	37.230	−5.44	5.81	1.70	1.10	0.0000	CWGB
P166ECSZ	242.359	36.307	−3.55	5.46	0.90	0.89	0.0400	CGB
P16XECSZ	243.254	36.828	−2.35	2.43	0.76	0.78	0.0000	CGB[d]
PASSECSZ	243.919	36.941	−2.78	1.99	0.52	0.48	−0.0100	CGB[d]
PERLCGPS	243.314	36.902	−3.64	0.29	0.33	0.30	0.0993	CGB[d]
POINCGPS	243.880	36.580	−3.89	0.25	0.38	0.33	0.1124	CGB[d]
POTBCGPS	238.065	38.203	−11.58	9.55	0.19	0.19	0.0191	–
QUINCGPS	239.056	39.975	−6.83	8.84	0.16	0.10	0.0018	SNGV
QUINNBAR	239.056	39.975	−5.51	6.61	0.77	0.47	0.0100	SNGV
QUINSNGV	239.060	39.970	−6.60	7.56	0.80	0.60	0.0000	SNGV
RAILCGPS	244.335	38.280	−3.34	0.00	0.43	0.36	0.1129	CGB
RATTNBAR	241.297	39.996	−7.22	2.92	2.08	1.28	−0.0300	NWGB[d]
RELACGPS	243.446	36.715	−3.42	0.89	0.38	0.34	0.1035	CGB[d]
REPOCGPS	243.532	36.840	3.14	0.60	0.26	0.24	0.0621	CGB[d]
RK59ECSZ	243.737	36.723	−1.88	2.63	0.50	0.46	0.0000	CGB[d]
ROGECGPS	242.915	36.218	−5.01	3.97	0.40	0.35	0.0988	SWGB
ROSSECSZ	243.461	36.697	−2.79	1.10	0.60	0.57	−0.0600	CGB
RUBYCGPS	244.877	40.617	−2.61	0.26	0.07	0.07	0.0322	CGB
RYANCGPS	243.350	36.316	−3.48	1.76	0.36	0.32	0.1002	SWGB[d]
S300CGPS	238.442	37.667	−11.00	8.53	0.62	0.58	0.0764	–
SHINCGPS	239.775	40.592	−6.41	4.89	0.07	0.07	−0.0001	NWGB[d]
SHOSCGPS	243.701	35.971	−4.20	0.59	0.37	0.33	0.1017	CGB
SHOSECSZ	243.739	36.943	−3.74	1.80	0.39	0.31	−0.0300	CGB
SKULCGPS	243.789	36.730	−3.69	0.23	0.38	0.34	0.1043	CGB[d]
SLIDCGPS	240.116	39.314	−10.36	6.12	0.09	0.09	−0.0120	NWGB
SMELCGPS	247.155	39.426	−2.92	0.32	0.08	0.07	0.0179	EGB
SMYCCGPS	244.413	36.320	−2.77	0.62	0.37	0.32	0.0960	CGB[d]
SND1YUCC	242.551	37.019	−2.49	3.64	0.53	0.61	−0.1079	SWGB
SPECECSZ	243.819	36.656	−2.49	2.39	0.54	0.51	0.0000	CGB[d]
SPRIECSZ	243.247	37.048	−2.53	2.30	0.50	0.47	0.0000	CGB[d]
SPRNSNGV	241.270	36.180	−8.98	9.33	1.30	0.60	0.0000	SNGV[e,f]
STOVECSZ	242.853	36.606	−1.69	3.37	1.02	0.96	0.0700	SWGB
STRICGPS	243.662	36.645	−2.75	1.23	0.38	0.33	0.1042	CGB[d]
SUTBCGPS	238.179	39.206	−10.81	8.12	0.16	0.16	0.0025	SNGV
SUTBSNGV	238.180	39.206	−9.92	8.75	2.00	1.30	0.0000	CGB
T15SECSZ	243.597	36.641	−2.58	1.61	0.75	0.73	−0.0700	SNGV[d]
T19SECSZ	242.417	36.232	−3.75	4.25	1.01	0.99	0.0300	SWGB
TATECGPS	243.426	36.932	−3.27	1.43	0.37	0.34	0.0995	CGB[d]
TIMBECSZ	243.539	37.088	−2.16	1.44	0.54	0.53	−0.0200	CGB
TINPYUCC	242.500	36.865	−2.39	4.19	0.53	0.61	−0.1044	SWGB
TIOGSNGV	240.750	37.930	−9.98	9.98	1.00	0.50	0.0000	SNGV[e,g]
TIVACGPS	243.770	36.935	−2.68	0.63	0.35	0.31	0.1008	CGB[d]
TONOCGPS	242.816	38.097	−3.42	2.25	0.35	0.31	0.0961	CWGB[d]
TUNGCGPS	241.742	40.403	−4.90	2.37	0.07	0.06	0.0041	NWGB
UCD1CGPS	238.249	38.536	−11.92	7.34	0.29	0.28	0.0575	SNGV
UCD1SNGV	238.250	38.536	−5.37	8.77	2.10	1.50	0.0000	SNGV
UPSACGPS	241.198	39.627	−6.41	3.57	0.09	0.09	−0.0177	NWGB[d]
V511ECSZ	242.134	36.061	−2.44	7.88	0.97	0.98	0.0500	SWGB
WAHOYUCC	243.677	36.781	−1.83	0.62	0.39	0.39	0.0345	CGB[d]
WELLECSZ	243.671	36.667	−3.85	1.22	0.61	0.58	−0.0500	CGB[d]
WGRDSNGV	241.850	37.270	−5.47	4.90	1.50	0.90	0.0000	CWGB

Table 1. (continued)

Station[b] ID	Longitude, deg	Latitude, deg	Estimate		Uncertainty		Correlation Coefficient	Region[c]
			East	North	East	North		
WHMEECSZ	243.677	36.781	−2.07	1.92	0.51	0.49	−0.0200	CGB[d]
WMTNSNGV	241.760	37.570	−3.44	4.85	1.00	0.80	0.0000	CWGB
X137ECSZ	242.720	36.402	−2.34	3.83	1.02	0.97	0.0700	SWGB
YUCCECSZ	243.515	36.940	−3.32	2.73	0.51	0.49	−0.0100	CGB[d]
			Sites Used to Define North America Reference Frame					
ALGOCGPS	281.929	45.956	0.27	−0.40	0.07	0.05	−0.0438	NOAM
AOMLCGPS	279.838	25.735	0.32	1.13	0.16	0.11	−0.0780	NOAM
BRMUCGPS	295.304	32.370	−0.88	1.46	0.13	0.07	−0.0882	NOAM
CASTCGPS	249.323	39.191	−0.67	0.67	0.07	0.06	0.0302	NOAM
CHURCGPS	265.911	58.759	0.33	−0.72	0.19	0.14	−0.0245	NOAM
DQUACGPS	265.710	34.111	0.14	1.26	0.11	0.09	−0.0057	NOAM
DRAOCGPS	240.375	49.323	1.53	1.72	0.06	0.06	0.0685	NOAM
DUBOCGPS	264.134	50.259	0.82	−1.05	0.41	0.25	−0.0170	NOAM
FERNCGPS	247.545	35.342	−1.53	1.28	0.40	0.33	0.1309	NOAM
FLINCGPS	258.022	54.726	−1.05	0.04	0.19	0.13	−0.0368	NOAM
FREDCGPS	247.501	36.988	−1.87	−0.47	0.39	0.32	0.1298	NOAM
GDACCGPS	257.820	37.775	0.29	0.49	0.09	0.07	0.0448	NOAM
GODECGPS	283.173	39.022	0.33	0.54	0.17	0.12	−0.0477	NOAM
HBRKCGPS	262.706	38.305	0.39	−1.26	0.11	0.09	0.0206	NOAM
HEBECGPS	248.627	40.514	−0.35	0.70	0.07	0.06	0.0440	NOAM
HKLOCGPS	264.137	35.683	−0.39	0.31	0.11	0.09	0.0048	NOAM
HVLKCGPS	260.893	37.651	0.34	−1.22	0.07	0.06	0.0245	NOAM
JTNTCGPS	259.023	33.017	0.48	−0.53	0.11	0.09	0.0260	NOAM
KELYCGPS	309.055	66.987	−0.63	−1.30	0.17	0.12	0.0624	NOAM
LMNOCGPS	262.519	36.685	0.12	1.52	0.11	0.09	0.0178	NOAM
MBWWCGPS	253.813	41.904	2.51	−0.31	0.87	0.69	0.0220	NOAM
MDO1CGPS	255.985	30.681	−0.34	0.47	0.07	0.06	−0.0404	NOAM
NDSKCGPS	264.362	37.381	0.49	−0.14	0.12	0.10	0.0121	NOAM
NLIBCGPS	268.425	41.772	0.69	0.68	0.10	0.06	−0.0016	NOAM
NRC1CGPS	284.376	45.454	−0.14	−0.15	0.13	0.08	−0.0138	NOAM
PATTCGPS	264.281	31.778	0.35	−0.43	0.12	0.09	−0.0083	NOAM
PIE1CGPS	251.881	34.302	0.30	−1.12	0.07	0.05	−0.0184	NOAM
PLTCCGPS	255.274	40.182	0.40	−0.43	0.10	0.08	0.0393	NOAM
PRCOCGPS	262.481	34.980	0.68	0.04	0.12	0.09	0.0208	NOAM
PRDSCGPS	245.707	50.871	0.65	−0.84	0.10	0.08	0.0591	NOAM
SCH2CGPS	293.167	54.832	−0.34	0.08	0.13	0.09	0.0167	NOAM
SOL1CGPS	283.546	38.319	1.13	1.00	0.35	0.26	−0.0518	NOAM
STJOCGPS	307.322	47.595	−0.97	0.50	0.11	0.07	−0.0351	NOAM
STRLCGPS	282.516	38.977	−2.23	2.95	0.34	0.21	−0.0624	NOAM
TCUNCGPS	256.391	35.085	0.41	−0.59	0.12	0.09	0.0463	NOAM
THU1CGPS	291.212	76.537	−1.09	−1.98	0.11	0.10	0.0591	NOAM
TMGOCGPS	254.767	40.131	−1.38	0.33	0.08	0.06	0.0572	NOAM
USNOCGPS	282.934	38.919	−0.63	−0.08	0.17	0.12	−0.0499	NOAM
VCIOCGPS	260.783	36.072	1.12	1.05	0.11	0.09	0.0295	NOAM
WES2CGPS	288.507	42.613	0.33	−0.31	0.10	0.06	−0.0567	NOAM
WLCICGPS	272.948	40.808	1.55	−2.48	0.30	0.18	−0.0037	NOAM
WLPSCGPS	284.530	37.937	−3.01	0.39	0.31	0.17	−0.0661	NOAM
WNFLCGPS	267.218	31.897	0.70	−0.60	0.13	0.11	−0.0056	NOAM
WSMNCGPS	253.650	32.407	−0.15	1.08	0.12	0.09	0.0463	NOAM
YELLCGPS	245.519	62.481	0.33	−0.99	0.10	0.08	0.0723	NOAM

[a]Estimates are in mm yr^{-1}.

[b]The last four characters of the site names indicate the network to which that site belongs: CGPS from CGPS data analyzed at SAO; YUCC from *Bennett et al.* [1997] and *Wernicke et al.* [1998]; NBAR from *Thatcher et al.* [1999]; SNGV from *Dixon et al.* [2000]; and ECSZ from *Gan et al.* [2000].

[c]Region refers to the geodetic province that site was assigned to for block motion and strain field estimations: CP, Colorado Plateau; CGB, central Great Basin; SNGV, Sierra Nevada–Great Valley; EGB, eastern Great Basin; SWGB, southwestern Great Basin; NWGB, northwest Great Basin; CWGB, west central Great Basin; and NOAM, North America interior. Region not specified indicates the site was not used for calculations.

[d]Sites used to investigate WGB shear parallel extension.

[e]Sites in interior SNGV.

[f]Sites in southern SNGV.

[g]Sites in northern SNGV.

this fact is reflected in the differences in the velocity uncertainties among these sites. In addition to these CGPS data, we also used the GAMIT software to analyze phase data from the southwestern Great Basin GPS campaigns described by *Bennett et al.* [1997] and *Wernicke et al.* [1998]. This campaign data set is comprised of seven observation sessions, each of 8–24 hours in duration, conducted approximately once per year between 1991 and 1999.

[8] GAMIT employs a model for doubly differenced carrier phase and a weighted least squares algorithm to derive estimates of site positions, satellite orbit parameters, Earth orientation parameters, time variable (piece-wise linear) azimuthally asymmetric atmospheric delays, and integer phase biases. For the purpose of estimating site velocities the fundamental output of our GAMIT data reductions are site position and Earth orientation parameter estimates and associated error variance-covariance matrices. For the CGPS sites we obtained (nominally) daily estimates for these parameters. For the campaign sites we obtained one set of estimates for each observation session. Changes in these parameters with time reveal motions of the Earth's surface. We used the GLOBK analysis software [*Herring*, 1999] to estimate site velocities from the complete set of GAMIT results. We estimated temporally constant velocities for all sites simultaneously using all of the available variance-covariance information, rather than fitting trends to individual sites separately, in order to exploit the intrinsic precision of the network solutions while at the same time insuring that all velocities share the same reference frame. In estimating the velocities we excluded all site position data whose evolution was obviously not well described by a constant velocity, except that we allowed for discrete offsets due to earthquakes, antenna changes, etc. A more detailed discussion of some of the more practical issues relating to our data analysis procedures (e.g., dealing with very large networks) is given by *Bennett et al.* [2002].

2.2. Definition of a Velocity Reference Frame

[9] To define a rotational reference, we fit a rigid North America plate model to 45 of the velocity estimates obtained from our GLOBK analysis. We distinguish between (1) the North America continent, which may experience ephemeral deformations that could bias geodetic inferences while not significantly contributing to permanent deformation (e.g., postglacial isostatic adjustment), and (2) the rigid North America plate model by referring to the North America plate model using the acronym NA. We used 45 sites located in the interior of North America to represent the NA plate. Residual velocities with respect to these sites provide us with a particular realization of the NA frame. Table 1 lists the residual velocities at these reference frame defining stations. This frame provides a convenient reference from which to describe qualitatively the velocity field, as we do later in this section. However, for the more quantitative analyses presented in following sections we employed the denuisancing technique of *Bennett et al.* [1996], which mitigates potential external reference frame biases. In our descriptions of the large-scale kinematics of the deformation field and the northern Basin and Range strain rate field in these latter sections we refer only to relative motions between (model) tectonic elements within or adjacent to the plate boundary zone or to velocity gradients, unless otherwise noted.

[10] The weighted root mean square (WRMS) scatter of the residual velocities at the 45 sites that we used to define the reference frame is 0.8 mm yr^{-1}. Note that this statistic is not a measure of systematic error in the reference frame determination. It represents the degree to which a rigid plate model approximates the GPS velocity estimates at a set of points that we deemed to be representative of the North America "plate."

2.3. Aggregation of Additional GPS Campaign Velocity Estimates

[11] We supplemented the GPS velocity estimates described above with velocity estimates from the campaign networks of *Thatcher et al.* [1999], *Dixon et al.* [2000], and *Gan et al.* [2000]. These velocity estimate sets were determined by regressing position data derived from GPS phase analyses using the GIPSY software and the point-positioning technique [*Zumberge et al.*, 1997]. All three of these data sets refer to unique realizations of the NA frame. We aligned these velocity estimate sets with our realization of the NA frame (described above) by modeling differences between site velocity estimates common to both our NA fixed solution and those of the data sets to be aggregated as the sum of translation rates and constant velocity gradients. We thus effectively estimated translation, rotation, scale, and shape change rates between velocity solutions such that the original differences among common site velocity estimates were minimized. This approach mitigates reference frame differences between the velocity solutions in addition to adjusting for possible spatially constant strain rate biases between data sets. In all three cases the inferred velocity transformations were dominated by marginally significant ≤ 1 mm yr^{-1} level translation rate estimates, indicative of small differences in the realizations of the NA frame, with relatively insignificant velocity gradient estimates, indicating insignificant differences in velocity scales, or other potential distortions among the velocity estimates sets.

2.4. Velocity Estimate Uncertainties

[12] The velocity uncertainties presented in this paper are of two varieties. The first variety is based on our least squares analyses of the GPS phase data following the standard least squares propagation of scaled observation errors. Our final velocity uncertainties were derived (together with the velocity estimates themselves) with the GLOBK software. In late 1999 we adopted a satellite elevation angle-dependent weighting scheme that is based on the actual scatter of the GPS phase residuals. We also applied an additional overall scaling to the resulting position estimates such that the square root of the chi-square per degree of freedom, i.e., the normalized root mean square (NRMS), of the scatter in daily position estimates about linear fits was on average near unity. A value of unity would be expected if the measurement errors were Gaussian and uncorrelated in time and the geodetic models employed

were exact. Uncertainties estimated in this way do not explicitly account for all potential deficiencies in the constant velocity model that we have adopted to estimate site velocities. Because the uncertainties do not account for potential modeling errors or data correlations, they only approximately characterize the true errors in the velocity estimates.

[13] Precise characterization of velocity accuracy requires a detailed knowledge of the errors in the geodetic and deformation models or the error spectrum of the GPS position data, neither of which are presently known. *Davis et al.* [2003] assessed velocity accuracy using a "whole error" approach, however, estimating an upper bound to the uncertainties of about 0.2 mm yr^{-1} for a subset of well-determined BARGEN velocities in Utah based on data from a slightly shorter period between epochs 1996.6 and 2000.9. The whole error method provides upper bounds for data sets of equal weight. Whole error estimates are upper bounds because they reflect the sum of observation errors and potential errors in simple models for crustal deformation, including any potential errors associated with the reference frame determination that are not common mode in nature. The "formal" uncertainties listed in Table 1 (for those sites that we analyzed with the GAMIT/GLOBK software, i.e., CGPS and (YUCC), from data for the slightly longer period between decimal year 1996.6 to 2001.3, range from $\sim$0.05 upward to $\sim$0.8 mm yr^{-1}. Our null hypothesis will be that our uncertainty estimates approximate the true uncertainties to within a factor of $\sim$2–3, generally consistent with the findings of *Davis et al.* [2003].

[14] The second variety of uncertainty that we report relates to the aggregated campaign data sets. For these data sets we adopted the uncertainties that were provided with the velocity estimates [*Thatcher et al.*, 1999; *Dixon et al.*, 2000; *Gan et al.*, 2000]. In all cases these estimates were scaled by factors determined appropriate by the respective groups who analyzed the raw data. Our assumption is that the reported uncertainties reasonably characterize the errors in these velocity estimates.

[15] We do not address the difficult problem of combining velocity estimate sets from different sources with unknown relative weights in this paper. Even if all of the data sets had been treated with the same software following the same strategy, we would still be confronted with unknown relative weights related to differing time spans and sampling frequencies of data collection, unknown effects of network equipment heterogeneity, the evolution of the GPS system and global tracking network, and other such complications in trying to assess velocity accuracy. The velocity uncertainties that resulted from our GAMIT/GLOBK analyses are typically smaller than those from the aggregated networks. The net effect of our choice is hence that we weight the aggregated data sets less strongly in our least squares analyses of large-scale plate boundary zone kinematics and strain rates in following sections. We demonstrate this effect below, showing that our deformation model parameter estimates are determined primarily by the CGPS data by repeating several of the model fits using only the CGPS velocity estimates (Table 1).

[16] Throughout the remainder of this paper we quote 3σ standard deviations on all model parameter estimates (i.e., relative microplate motions and strain rates). As we will demonstrate through numerical testing, this scaling appears to account adequately for potential model and data errors not characterized by the formal standard deviations. Because this factor is intended to account for the effects of both model and data uncertainties on our model parameter estimates, we do not scale the GPS velocity (data) uncertainties by this factor of 3, one-dimensional ("x–y") data plots show formal 1 standard deviation error bars; two-dimensional data vector plots show 95% error ellipses (i.e., $\sim$2.45 times the formal 1 standard deviations).

2.5. Description of the Velocity Field

2.5.1. Velocities in the NA Frame

[17] Previous geodetic investigations into the distribution of deformation across the northern Basin and Range province have adopted NA fixed reference frames [*Dixon et al.*, 1995; *Bennett et al.*, 1998, 1999; *Thatcher et al.*, 1999; *Dixon et al.*, 2000]. Several basic observations, which have been reported to some extent or another in these previous space geodetic studies, are also apparent in Figure 2. Sites east of the Intermountain seismic belt on the Colorado Plateau (Figures 1a and 1b) move very slowly with respect to the NA frame. Horizontal rates of site motion increase more or less monotonically across the northern Basin and Range from the Colorado Plateau to the Sierra Nevada–Great Valley microplate. A systematic change in the azimuth of site motions is evident across central Nevada. Whereas west directed site motions in the northeast are indicative of crustal extension across the north trending normal faults of the Basin and Range province, a transition zone, comprising a gradual swing in azimuth from west to northwest directed motions, occurs near longitude 116°W, about 100 km east of where the central Nevada seismic belt crosses the northern Basin and Range province (Figures 1a, 1b, and 2). This transition culminates in west-northwest to northwest directed site motions on and west of the Sierra Nevada, more westerly than, but roughly parallel to, the direction of Pacific plate motion with respect to stable North America.

2.5.2. Colorado Plateau

[18] The Colorado Plateau, which is adjacent to the northern Basin and Range province on the east (Figure 1a), is generally assumed to be an uplifted but relatively undeformed crustal block. Paleomagnetic data suggest significant rotation of the plateau with respect to the NA frame since the Jurassic, although the timing of this rotation is not well resolved [*Steiner and Lucas*, 2000]. Contemporary strain rate estimates across the Rio Grande rift, which borders the Colorado Plateau on the east, are typically $\leq$1 mm yr^{-1} [e.g., *Savage et al.*, 1980] but are consistent with slow present-day rotation of the plateau with respect to the continental interior. To date, however, geodetic measurements are insufficient to constrain tightly modern deformation of this block or its rotation with respect to the NA frame. *Argus and Gordon* [1996] argued for a loose upper bound on CP-NA relative motion of 4–5 mm yr^{-1}, for

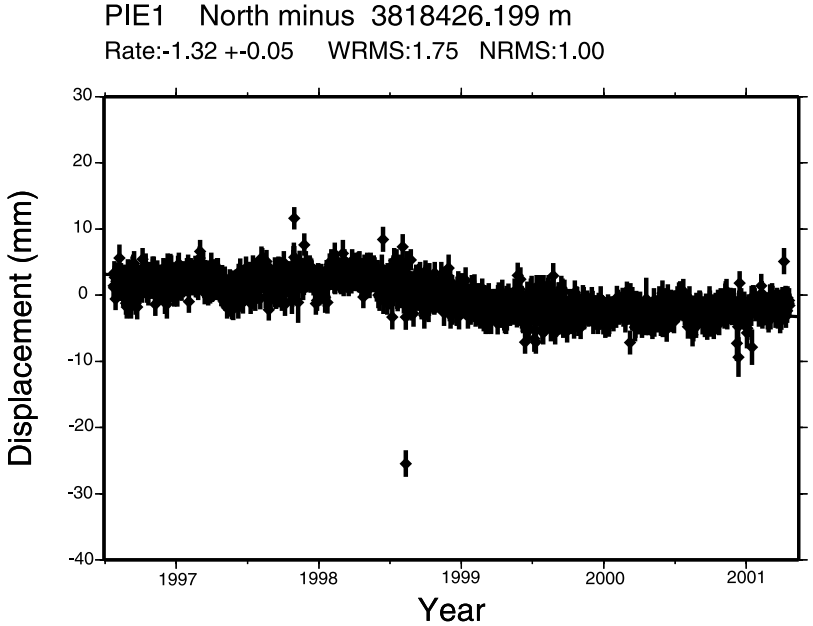

Figure 3. Time series of the north component of position for IGS site Pietown (PIE1) exhibiting accelerated motion during the period from about 1998 to 1999.5. Error bars represent 1 standard deviation. Although it is not possible to determine unequivocally the source of this accelerated motion, or apparent accelerated motion, this behavior is not seen in any of the other Colorado Plateau sites. Perhaps this time series records transient deformation associated with subterranean magma movement near Socorro, New Mexico. This site was not used in our deformation analyses.

example, based on sparse VLBI station coverage. Although GPS sites on the Colorado Plateau do not appear to move appreciably with respect to the NA plate in a root mean square sense when analyzed together with a large set of stations distributed throughout the North America interior (relative to the precision with which we can constrain deformation of the NA plate itself) [*Bennett et al.*, 2002] (see also Table 1), this does not preclude small but coordinated relative motion between CP sites and the rest of NA, which could potentially be indicative of rigid block motion with respect to the NA frame. In this paper, we distinguish between the actual physiographic Colorado Plateau, which may be internally deforming at some level, and the hypothetical rigid Colorado Plateau block by referring to the rigid model using the acronym CP.

[19] Ten GPS sites (Table 1) are now located on the Colorado Plateau, east of the major tectonic elements of the Pacific–North America plate boundary zone (Figures 1a, 1b, and 2). We do not include IGS site PIE1, located on the Colorado Plateau just west of the Rio Grande Rift, in our analyses because time series of site position for this station are clearly not well modeled by a constant velocity (Figure 3). PIE1 is located about 200 km from crustal magma bodies near Socorro, New Mexico. *Larsen and Reilinger* [1986] presented evidence from repeated first-order leveling surveys for broad ongoing deformation associated with magma movement in this region. *Fialko and Simons* [2001a] report evidence for several centimeters of uplift near Socorro between 1992 and 1999 from interferometric synthetic aperture radar data. Crustal deformation associated with subterranean magma movements can be very large in amplitude and highly spatially and temporally variable [e.g., *Dixon et al.*, 1997; *Aoki et al.*, 1999]. However, the cause of the apparent change in velocity at PIE1 is difficult to assess because of the lack of neighboring stations, which makes it difficult if not impossible to determine whether or not this apparent motion is representative of subsurface magmatic movements or whether it is indicative of an instability in the electrical environment, monumentation at this site, or some other unknown cause.

[20] With respect to the North America reference frame (Table 1) the weighted mean motion of the Colorado Plateau sites (Table 2) is 0.9 ± 0.1 mm yr^{-1}, N51 ± 9°W. The NRMS of this fit is 0.7, less than unity, suggesting that the scaled uncertainties slightly overestimate the combined effects of model error and observation noise. The WRMS scatter of the residual velocities is 0.3 mm yr^{-1}, almost a factor of 3 smaller than the residual scatter associated with the fit to the NA plate. To test how sensitive this result is to the aggregated velocities, we repeated this analysis using only the CGPS sites on the CP block, finding a net motion of 0.9 ± 0.1 mm yr^{-1} oriented N45° ± 9°W, with a NRMS fit of 0.9 and a WRMS residual scatter of 0.2 mm yr^{-1}. The

Table 2. Microplate Translations With Respect to North America

Microplate	Rate, mm yr^{-1}	Azimuth, deg	NRMS	WRMS, mm yr^{-1}
CP	0.9 ± 0.1	N51° ± 9°W	0.7	0.3
CGB	3.56 ± 0.09	N80° ± 1°W	0.9	0.6
SNGV	12.4 ± 0.2	N47.0° ± 0.9°W	1.6	1.3

Table 3. Microplate Euler Poles With Respect to North America

Microplate	Longitude	Latitude	Rate, deg Myr^{-1}	NRMS	WRMS, mm yr^{-1}
CP	253° ± 4°E	42° ± 2°N	0.11 ± 0.09	0.5	0.2
CGB	268° ± 40°E	74° ± 20°N	0.05 ± 0.02	0.9	0.6
SNGV	143° ± 50°E	56° ± 10°N	0.14 ± 0.06	1.6	1.3

difference between these block motion estimates, in both magnitude and direction, is less than 1 standard deviation. Addition of the aggregated campaign data does not noticeably reduce the parameter estimate uncertainties.

[21] A CP-NA Euler vector (253° ± 4°E, 42° ± 2°N, 0.11° ± 0.08° Myr^{-1}) (Table 3) fits the velocity estimates at these same 10 sites only slightly better than that for the translating block model, with a NRMS fit of 0.5 and a WRMS residual scatter of 0.2 mm yr^{-1}. A Euler vector fit to the subset of these velocities that are based on CGPS data only (254°E, 42°N, 0.10° Myr^{-1}) results in a NRMS fit of 0.6 and a WRMS residual scatter of 0.2 mm yr^{-1}. The small difference in chi-square between the Euler vector and translating block models may suggest that a rotating microplate model does a slightly better job of representing rigid CP-NA motion. The significance of this reduction is difficult to assess, however, as F tests and other statistical methods of model comparison technically apply only to lesser/fuller model pairs and therefore do not discriminate between models of different natures. If the Colorado Plateau is deforming or rotating, it does so such that the scatter among the velocities at these 10 locations is $\leq$0.3 mm yr^{-1}.

[22] To further assess the rigidity of the CP, we estimated constant velocity gradients in addition to a translation rate from these same 10 velocity estimates; although strain within the block would not necessarily preclude rigidity (i.e., observed strain could be elastic and recoverable), the absence of significant strain would bound distributed plastic (nonrecoverable) deformation. Our velocity estimates are listed in Table 4. The NRMS of the fit of this velocity gradient model was 0.5, and the WRMS scatter of the residual velocities was 0.2 mm yr^{-1}, identical to the values obtained for the fits of the Euler vector models described above. We separated the resulting velocity gradient tensor into the sum of a symmetric strain rate tensor and a rotation rate tensor, finding that all components of the strain rate tensor are small (sub–nstr yr^{-1} level) and statistically insignificant. This supports the notion of little to no appreciable modern deformation of the Colorado Plateau. The rate of rotation is 0.1° ± 0.1° Myr^{-1} clockwise about the centroid of the network. Figure 4 shows north and east components of velocity for these sites as a function of north and east distance, respectively. Superimposed on the data are the velocity gradient estimates that we obtained. The plots have been corrected for out of plain variation using the procedure described in a later section.

Table 4. Velocity Gradient Tensor Estimates[a]

Strain Domain	Velocity Gradient^{-1} nstr yr^{-1}			
	$\dot{\varepsilon}_{11}$	$\dot{\varepsilon}_{12}$	$\dot{\varepsilon}_{21}$	$\dot{\varepsilon}_{22}$
CP	1 ± 4	2 ± 2	−1 ± 3	−1 ± 1
CGB	0 ± 2	−0.9 ± 0.6	−5 ± 2	−0.1 ± 0.6
SNGV	29 ± 5	−4 ± 2	−18 ± 4	0 ± 2
EGB	7 ± 3	2 ± 2	1 ± 3	2 ± 2
NWGB	9 ± 1	7 ± 2	−36 ± 1	−4 ± 2
CWGB	−6 ± 5	−4 ± 11	−25 ± 5	−3 ± 9
SWGB	−11 ± 10	3 ± 5	−57 ± 9	−10 ± 5
WGB	−13 ± 5	−1.4 ± 0.6	−19 ± 5	8.5 ± 0.5

[a]CP, CGB, SNGV, EGB, SWGB, NWGB, CWGB, and WGB refer to the domains in which the strain field was assumed to be constant in the various estimations. See the text for the details about the strain calculations and stations used to define the domains. The 1 and 2 directions vary with domain: CP and CGB, 1 = E, 2 = N; SNGV, 1 = N50°E, 2 = N40°W; EGB, 1 = N6°E, 2 = N84°W; and NWGB, CWGB, SWGB, and WGB, 1 = N53°E, 2 = N37°W.

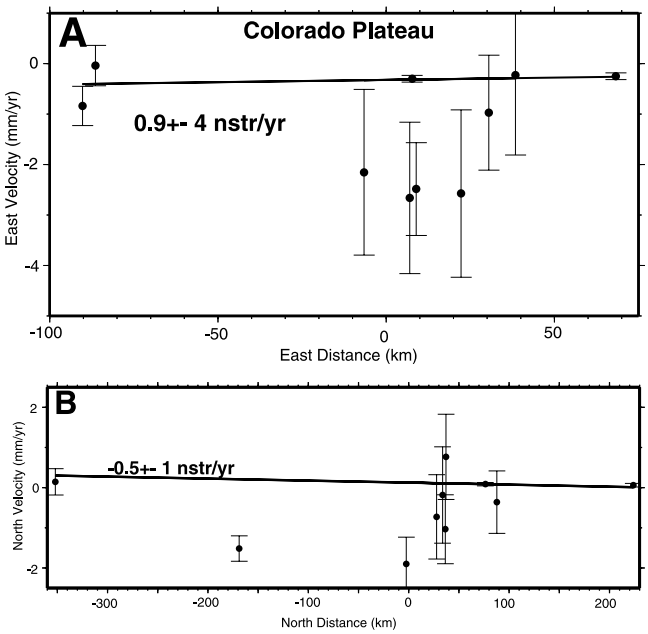

Figure 4. (a) East and (b) north components of velocity for sites on the Colorado Plateau (CP) as functions of east and north distance, respectively. Velocities refer to the North America reference frame. Error bars represent 1 standard deviation. Both data and model velocity gradients have been corrected using equations (4) and (5). We observe very little relative motion among these stations, consistent with the notion of a rigid microplate. The origin of the horizontal axis corresponds to the location of the square in Figure 2.

[23] Although these data place constraints on the rigidity of the CP, the question of whether or not these analyses are indicative of secular CP-NA relative motion is difficult to assess since our realization of the NA frame could be biased by numerous large-scale effects that are transient on geological timescales, such as postglacial rebound, or other effects, such as strain associated with diffuse plate boundary zones. The rate that we estimate from the translating CP model ($\sim$0.9 mm yr^{-1}) is similar in magnitude to the WRMS scatter of the residual velocities at the 45 sites used to define the NA frame ($\sim$0.8 mm yr^{-1}). On the other hand, it is not yet clear to what extent NA model misfit reflects

local processes (which do not significantly affect the NA frame determination [cf. *Bennett et al.*, 2002]) or large-scale effects that could potentially bias the frame determination. A more complete analysis than we here have space for will be necessary in order to resolve these issues. As mentioned above, however, the quantitative analyses that follow this section do not depend on our realization of the NA frame, unless otherwise noted.

[24] From the perspective of the Colorado Plateau reference frame the GPS velocity field is qualitatively very similar to velocities in the North America fixed reference shown in Figure 2. We therefore do not include an extra figure showing site velocities in the CP reference frame in this paper.

2.5.3. Sierra Nevada–Great Valley Microplate

[25] As with the Colorado Plateau, the Sierra Nevada–Great Valley region, which is adjacent to the northern Basin and Range province on the west (Figure 1a), is widely regarded as a rigid block or microplate [e.g., *Argus and Gordon*, 1991]. Recent geodetic investigations support the rigid microplate hypothesis to an extent [*Dixon et al.*, 2000], finding that GPS site velocities for the interior region of the microplate are consistent with rigid body translation with respect to NA at the sub–mm yr^{-1} level. Additional sites to the east and west of this interior region reveal strain within the block. However, this strain is not necessarily inconsistent with the notion of a long-lived rigid block because it may be due to the effects of elastic (i.e., recoverable) strain accumulation associated with the greater San Andreas fault system to the west and the eastern California shear zone to the east and/or transient postseismic effects associated with the great 1906 San Francisco, 1857 Fort Tejon, and/or 1872 Owens Valley earthquakes (Figure 1a). In this paper we distinguish between the actual Sierra Nevada and Great Valley regions, which may be internally deforming at some level, and the hypothetical rigid Sierra Nevada–Great Valley microplate by referring to the rigid model using the acronym SNGV.

[26] A number of sites in Figure 2 and Table 1 lie within the region typically regarded as the SNGV microplate region. Because of the overlap in site velocity estimates among the aggregated velocity solutions, these sites yield 20 velocity estimates at 14 locations (Table 1). The weighted mean of all 20 of these velocities is 12.4 ± 0.2 mm yr^{-1}, oriented N47.0° ± 0.9°W (Table 2), providing an estimate of SNGV-NA relative motion. The NRMS fit of this model to these velocities is 1.6, greater than unity and significantly larger than the analogous fit we obtained for the translating model to the Colorado Plateau velocities. This is likely indicative of deformation of the SNGV, assuming that the CP results described above (NRMS values ~0.5–0.9) reflect on the precision of the entire data set, including SNGV sites. The WRMS scatter of the residuals to this fit is 1.3 mm yr^{-1}, again significantly larger than that for the corresponding CP model. To test the sensitivity of this result to the aggregated velocities, we repeated this analysis using only the CGPS sites on the SNGV microplate, finding a net motion of 12.5 ± 0.2 mm yr^{-1} oriented N47.2° ± 0.9°W, with a NRMS fit of 2.3 and a WRMS residual scatterof 1.3 mm yr^{-1}. By comparison with the solution based on the full set of data, in terms of both the velocity estimates and their uncertainties the motion of the SNGV block is predominantly determined by the CGPS data.

[27] The best fit Euler vector to the full SNGV data set (143° ± 50°E, 56° ± 10°N, 0.14° ± 0.06° Myr^{-1}) (Table 3) results in a NRMS fit of 1.6 and a WRMS scatter of 1.3 mm yr^{-1}, whereas the Euler vector fit to the CGPS subset (111°W, 58°N, 0.18° Myr^{-1}) furnishes a NRMS fit of 2.3 and a WRMS residual scatter of 1.3 mm yr^{-1}. That these statistics are identical to those for the translating block model indicates that the block model fits these data as well as the microplate model, consistent with the results of *Dixon et al.* [2000].

[28] Our rate estimate of 12.4 mm yr^{-1} with respect to North America is significantly smaller than the 13–14 mm yr^{-1} estimate of *Dixon et al.* [2000]. To determine whether this difference is caused by differences in realizations of the NA frame, we reestimated the motion of the SNGV microplate using only those stations used by *Dixon et al.* [2000]. The weighted mean of the velocity estimates of these stations in our realization of the NA frame is 13 ± 1 mm yr^{-1} oriented N43° ± 5°W, with a NRMS fit of 0.3 and a WRMS scatter of 0.9 mm yr^{-1}, whereas the mean of the original *Dixon et al.* [2000] data set is 14 ± 1 mm yr^{-1} oriented N47° ± 5°W, with a NRMS fit of 0.3 and a WRMS scatter of 1.0 mm yr^{-1}. Hence the rate difference is partially explained by reference frame differences. The remainder of the difference results from our use of additional sites, such as site QUIN. Including site QUIN in the calculation, for example, reduces these rate estimates by 0.7–0.8 mm yr^{-1} with no significant change to the orientations.

[29] Following *Dixon et al.* [2000], we also refit these rigid body motion models to a subset of sites located in the interior of the block to assess the effects of strain accumulation associated with block-bounding fault zones. For this test we use 11 velocity estimates from eight sites (Table 1). From the translating SNGV model's fit to these sites we obtain a rate of 12.6 ± 0.2 mm yr^{-1}, oriented N48.2° ± 0.9°W. The NRMS fit of 1.3 is a slight improvement over the fit to the larger data set, and the rate and azimuth estimates are consistent with estimates based on the full SNGV velocity data set at 2 standard deviations. The WRMS scatter of the residual velocities is 1.0 mm yr^{-1}, as for the fit to the larger data set. The Euler vector fit to the smaller data set (217°E, −10°N, 0.20° Myr^{-1}) is no better than the translation model, with a NRMS fit of 1.3 and a WRMS scatter of 1.0 mm yr^{-1}. The improvement in misfit when using the interior subset relative to the full data set is likely indicative of deformation of the SNGV region associated with elastic strain accumulation on block-bounding faults, such as the San Andreas fault.

[30] Another test of SNGV rigidity, again following *Dixon et al.* [2000], is to fit separate models to velocities in the north and the south of the microplate. If there is no significant difference between estimated block motions between these regions, then this would support the rigid

block hypothesis. We define a northern region by eight velocities at five stations (Table 1) and a southern region by seven velocities at seven stations (Table 1). The weighted average velocity of the northern set is 12.5 ± 0.2 mm yr^{-1} oriented N49° ± 1°W (NRMS = 1.4 and WRMS = 0.9), whereas that of the southern set is 14.5 ± 0.6 mm yr^{-1} oriented N49° ± 2°W (NRMS = 0.8 and WRMS = 1.3). Rate estimates for the north and south differ by nearly 4σ although the block motion estimates' directions are essentially identical. The results for the northern subset of velocities are within about 1σ of those for the entire velocity set as well as with the interior set of stations.

[31] Because there is no evidence in the geology of the SNGV region for permanent deformation within the interior of this block, that the southern sites appear to move more rapidly than those to the north is not likely to reflect deformation processes that result in permanent deformation. To assess further deformation of the SNGV region, we estimated a constant velocity gradient in addition to a translation rate from the subset of 20 SNGV velocities (Table 4). The NRMS of the fit of this model was 1.6, and the WRMS of the scatter about this fit was 1.3 mm yr^{-1}, comparable to the fits of the translating block and rotating microplate models tested above. We rotated the velocity gradient tensor into a coordinate system with one axis pointing N40°W, generally parallel to the strike of the San Andreas fault at this latitude. Figure 5a shows N50°E and N40°W components of velocity with respect to North America as functions of N50°E distance. As Figure 5a illustrates, there is a rather large 18 ± 4 nstr yr^{-1} increase in N40°W directed motion from northeast to southwest across the SNGV region, consistent with right lateral shear, presumably associated with the northwest striking fault zones that bound the SNGV region. N50°E components of velocity decrease at a rate of 29 ± 5 nstr yr^{-1} from northeast to southwest. A similar analysis using only the interior subset of sites yields significantly reduced strain rates, none of which are statistically significant. For both cases there is no appreciable variation in N40°W velocity with N40°W distance. Hence the velocity difference between the northern and southern subsets of sites is a reflection of station distribution, with the southern translation rate estimate being heavily influenced by sites LINDCGPS and ISLKCGPS, which lie southwest of the SNGV network centroid.

[32] Because there is only a small improvement to the fit when using subsets of the SNGV velocities and because the implications for block motion are generally comparable for all but the southern of the subset solutions (i.e., they are equivalent to within about 1σ), it is difficult to favor one of the subsets of data over the full SNGV velocity data set. We therefore opt to use the complete set of SNGV velocities to represent SNGV motion in following sections.

[33] Figure 6 shows the Basin and Range velocity field with respect to the SNGV frame defined by this 14-station (20-velocity) data set, providing a different perspective on the velocity data shown in Figure 2. From the SNGV frame, site motions across the western Great Basin are oriented more northerly than the direction of SNGV-NA relative motion by as much as ∼15° (Figures 2 and 6). These velocities are, however, very close in orientation to the direction of P-NA relative motion and well within the range of azimuths of strike slip faults in the region comprising the Walker Lane belt (Figures 1a and 1b). Velocities in the western Great Basin are roughly parallel to one another and increase in magnitude northwestward to a value of 8–10 mm yr^{-1} and do not appear to vary appreciably to the east of longitude ∼116.5°W (Figure 6). These velocities thus appear to reveal a shear zone across the western Great Basin region (blue vectors of Figure 6 defining a region that contains, but is larger than, the ECSZ and Walker Lane belt (Figure 1b)). The change in velocity gradient and regional strain rate about 100 km east of the central Nevada seismic belt corresponds to the relatively abrupt change in orientation of velocities relative to North America apparent on Figure 2, with more northwesterly velocities to the west [*Bennett et al.*, 1998, 1999; *Thatcher et al.*, 1999].

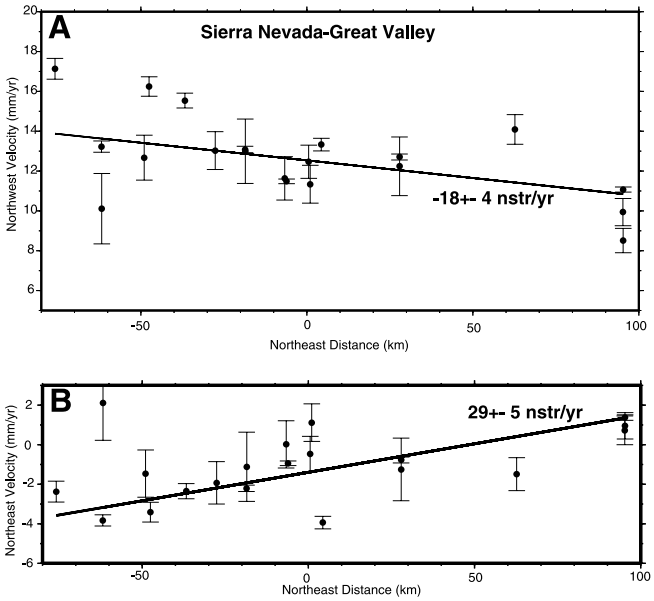

Figure 5. (a) Northwest and (b) northeast components of velocity for sites on the Sierra Nevada–Great Valley (SNGV) microplate as functions of northeast distance. Velocities refer to the North America reference frame. Error bars represent 1 standard deviation. Both data and model velocity gradients have been corrected using equations (2)–(5), accordingly. Significant variation in both components of deformation across the microplate are indicative of elastic strain associated with the fault zones that bound the microplate to the southwest and northeast, rather than with the permanent deformation of the microplate. The origin of the horizontal axis corresponds to the location of the square in Figure 6.

2.5.4. Central Great Basin

[34] Although Quaternary faulting is prevalent, previous workers have proposed that the central Great Basin may behave as a rigid or only very slowly deforming block

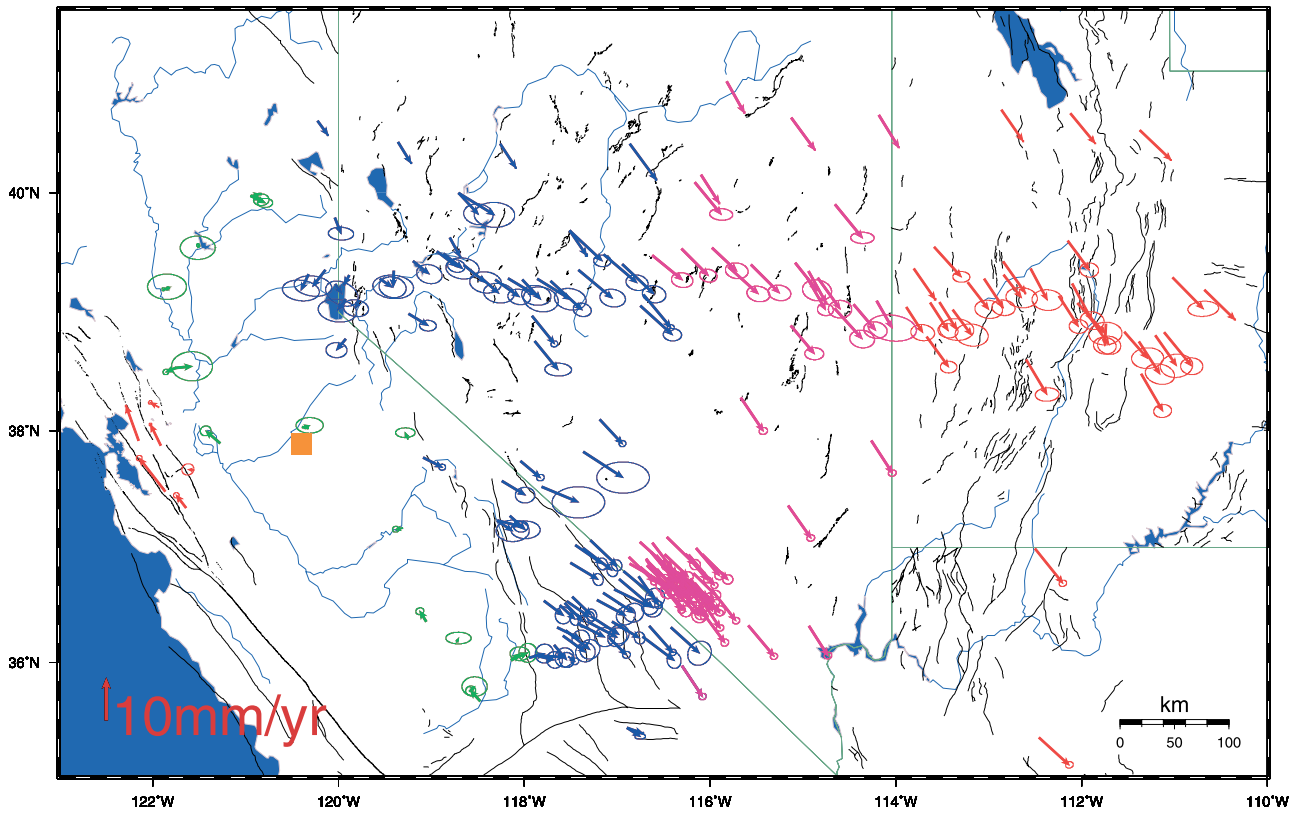

Figure 6. GPS velocities with respect to the Sierra Nevada–Great Valley (SNGV) microplate fixed reference frame. Error ellipses represent the 95% confidence level. Green vectors show the sites used to define the velocity reference frame. Blue vectors reveal a shear zone within the western Great Basin region. Pink vectors reveal a region in which deformation is comparatively small. Quantitative analyses of these velocities are presented later in the paper. The orange square shows the average geographic location of sites that we used to define the Sierra Nevada–Great Valley microplate and represents the origin of the horizontal axes in Figure 5.

principally on the basis of the locations of active seismic belts (Figures 1a and 1b) [e.g., *Smith*, 1977]. *Dixon et al.* [1995, 2000] interpreted space geodetic measurements from rather sparse networks using a vector summation approach to infer that the majority of northern Basin and Range deformation occurs along the boundaries of the Great Basin. However, more dense sets of GPS measurements from within the northern Basin and Range province demonstrate that a significant amount of deformation occurs across broad zones between the central Nevada seismic belt and the eastern face of the Sierra Nevada [e.g., *Bennett et al.*, 1998; *Thatcher et al.*, 1999] and in western Utah [*Niemi et al.*, 2003; *Friedrich et al.*, 2003]. Strain accumulation between these regions, throughout the longitude band 114°–116.5°W, is considerably smaller [e.g., *Savage et al.*, 1999; *Thatcher et al.*, 1999], although anomalous but small motions east of the central Nevada seismic belt and eastern California shear zone, which are perhaps indicative of transient deformations associated with relaxation processes following large earthquakes within this belt, have also been reported [*Wernicke et al.*, 1998, 2000]. As we have done for the CP and SNGV regions above, we distinguish between the actual central Great Basin region, which may be deforming, and the hypothetical rigid central Great Basin, by referring to the rigid model by the acronym CGB.

[35] The mean motion of a set of 65 stations in the CGB roughly occupying the longitude band 114°–116.5°W (Table 2) is 3.56 ± 0.09 mm yr^{-1} oriented N80° ± 1°W. The NRMS of this fit is 0.9, and the WRMS of the scatter about this fit is 0.6 mm yr^{-1}. To assess the contribution of the aggregated campaign data, we reestimated the mean velocity using only CGPS sites, finding a mean of 3.57 ± 0.09 mm yr^{-1} oriented N82° ± 2°W. The NRMS of this fit is 1.1, and the WRMS scatter about this fit is 0.5 mm yr^{-1}. The mean velocity for this region is therefore largely determined by the CGPS data. Variation among the north components (WRMS = 0.4 mm yr^{-1}) is slightly smaller than for the east components (WRMS = 0.7 mm yr^{-1}) for the more precise CGPS subset. This is consistent with the possibility that some of the observed scatter results from deformation associated with the roughly north trending fault zones within and adjacent to the CGB region, but it could also reflect GPS positioning precision, which is inherently

slightly better in the north because of the geometry of the GPS satellite constellation.

[36] The best fit Euler pole for these stations (268° ± 40°E, 74° ± 20°N, 0.05° ± 0.02° Myr^{-1}) (Table 3) fits these same data no better, with a NRMS of 0.9 and a WRMS of 0.6 mm yr^{-1}. The best fitting Euler pole to the CGPS data only (258°E, 71°N, 0.06° Myr^{-1}) similarly provides a comparable fit (NRMS = 1.1 and WRMS = 0.6 mm yr^{-1}).

[37] As with the CP and SNGV regions analyzed above, we also fit a constant velocity gradient model in addition to a translation rate. The NRMS fit of this model to the data is 0.8, and the WRMS scatter about this fit is 0.5 mm yr^{-1}, equal to or only slightly smaller than for the rigid models considered above. We found a 5 ± 2 nstr yr^{-1} increase in the north components of velocity with distance from east to west, whereas other components of the velocity gradient tensor are significantly smaller (Table 4 and Figure 7a). This deformation is not consistent, however, with strain accumulating on the north trending basin-bounding normal faults in the CGB region. More likely, it reflects a small amount of northwest directed right lateral shear spilling over from the faults in the western Great Basin region to the west. Hence, although prevalent Quaternary faulting in the central Great Basin precludes the notion of a long-lived rigid CGB microplate, strain accumulation on these faults is presently below the level of resolution of these data. Geodetically therefore this region is effectively a microplate.

[38] Figure 8 shows velocity estimates with respect to the CGB fixed reference frame. As was evident from the SNGV fixed frame (Figure 6), velocities across the western Great Basin appear to define a shear zone. Velocities of sites on the SNGV block are parallel to the azimuth of the San Andreas fault zone and to the direction of Pacific–North America relative plate motion (Figure 1a). Across the eastern boundary of the Great Basin there is a rapid increase in east directed velocities as the Intermountain seismic belt and greater Wasatch fault zone are crossed in Utah.

2.5.5. Reflections on the Resolving Power of the GPS Velocity Field

[39] GPS data from the CP are consistent with long-term rigid microplate behavior. We observe no deformation within this region at the level of <1 mm yr^{-1}. In contrast, the SNGV region experiences velocity variation with distance in the N50°E direction. However, on the basis of the lack of permanent deformation recorded by the geology and on the pattern of velocity variation we attribute this observation to elastic strain associated with block-bounding fault zones such as the San Andreas and the fault zones of the eastern California shear zone. We also observe small velocity variations in the CGB, which we attribute to elastic strain associated with right lateral shear in the western Great Basin region. Slip on the north trending normal faults of the CGB is presently below the resolution of the GPS data. In this sense we consider the CGB region as a "geodetic microplate," keeping in mind that prevalent Quaternary faults in this region preclude the notion of a long-lived rigid tectonic microplate.

[40] Small deformations and possible relative rotations notwithstanding, tests using various subsets of data indicate that our block motion estimates do not appear to be biased appreciably by such effects. Nonrigid deformations of these regions, which were not accounted for in some of the models considered above, contribute somewhat to the RMS values that we calculated to assess the fits of these models to the data. For all these regions considered, however, a

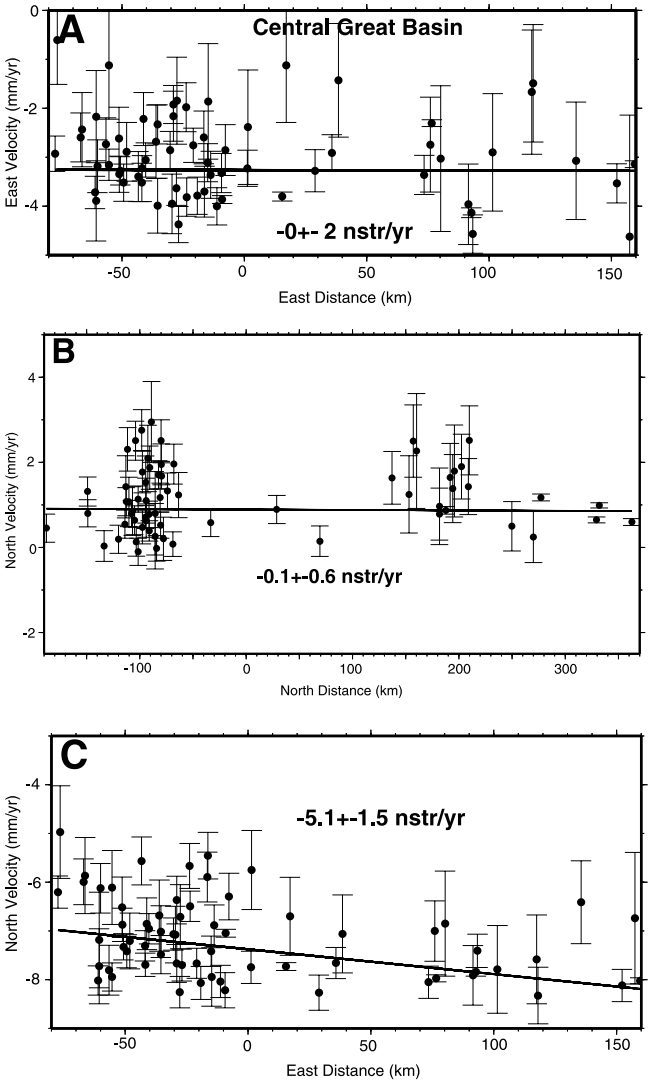

Figure 7. (a) East velocity versus east distance, (b) north velocity versus north distance, and (c) north velocity versus east distance for sites in the central Great Basin region (CGB). Velocities refer to the North America reference frame. Error bars represent 1 standard deviation. Both data and model velocity gradients have been corrected using equations (2)–(5), accordingly. Significant variation in north components of velocity from east to west Figure 7c is not consistent with extension on the north trending normal faults within the CGB region. This variation is more likely related to elastic strain associated with right lateral shear in the western Great Basin. The origin of the horizontal axes corresponds to the location of the square in Figure 8.

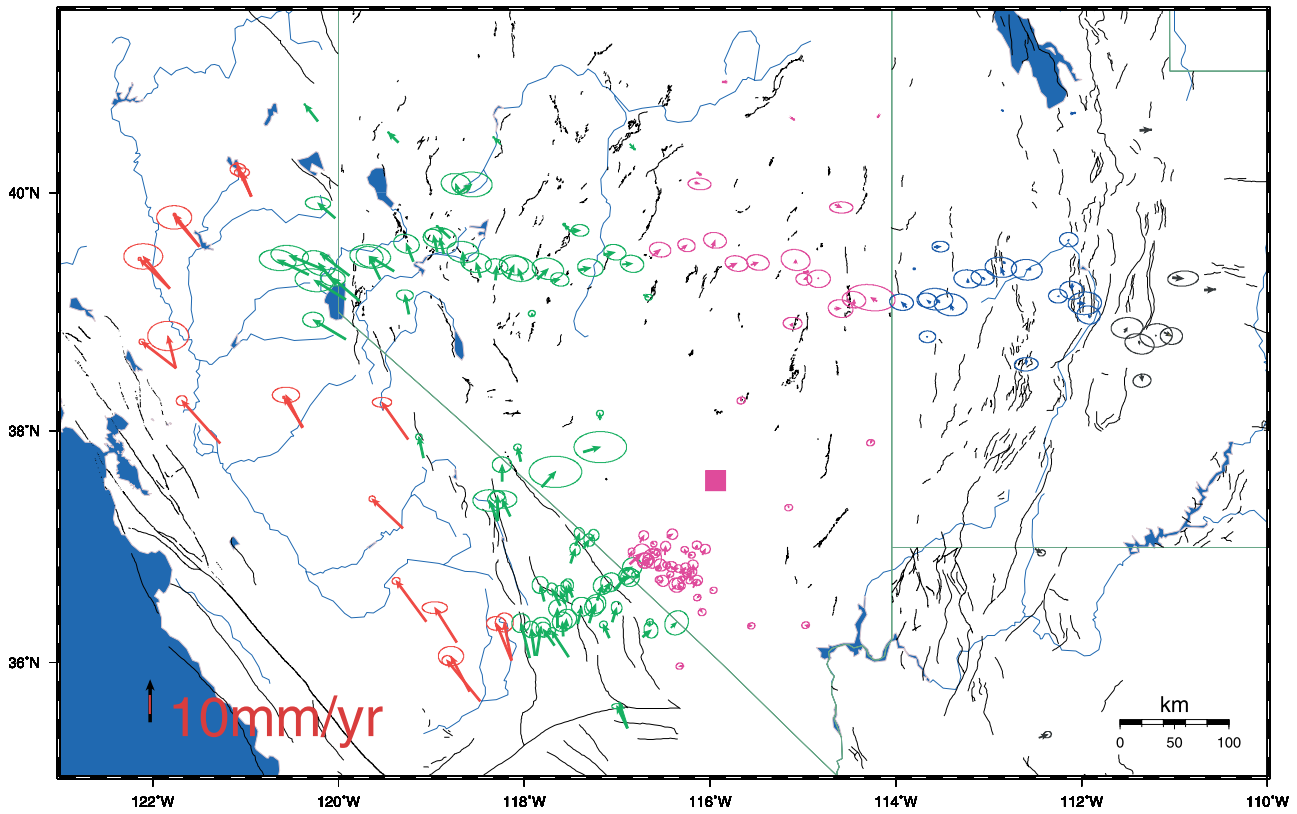

Figure 8. GPS velocities with respect to the central Great Basin (CGB) fixed reference frame. Error ellipses represent the 95% confidence level. Pink vectors show the velocities of sites used to define the velocity reference frame. The Colorado Plateau region (black) clearly moves eastward relative to the CGB frame. The Sierra Nevada–Great Valley (SNGV) region (red) translates northwest with respect to the CGB. Blue and green vectors delineate eastern and western Great Basin regions, respectively, which accommodate the relative motions of the more rigid regions. The pink square shows the average geographic location of sites that we used to define the CGB microplate and represents the origin of the horizontal axes in Figure 7.

constant velocity gradient model did not reduce the RMS values appreciably relative to the rigid models. With the exception of the SNGV microplate, which is the most rapidly deforming of the three regions and for which, in many instances, we obtained NRMS values significantly larger than unity, the RMS values that we obtained were consistent with the uncertainty scaling that we applied.

2.6. Large-Scale Kinematics

[41] In the previous section, we used subsets of the GPS velocity field (Figure 2) to investigate the overall kinematics of three regions, which have previously been hypothesized to be relatively underforming on the basis of seismological and/or geological considerations. We found that to a reasonable approximation these regions may geodetically be considered as undeforming blocks. In this section, we quantify the large-scale kinematics of the deformation field across the northern Basin and Range province as a whole by using these subsets to estimate rigorously the relative rigid body motions of these regions. Rather than simply differencing the results obtained above, we use all of the velocity data in a simultaneous estimation for rigid body motions, which allows us to enforce a velocity vector closure constraint. That is, we force the solution to be such that $V_{SNGV-CP} = V_{SNGV-CGB} + V_{CGB-CP}$, where $V_{SNGV-CP}$ represents the velocity of the SNGV block with respect to the CP block, etc. The procedure that we employ to achieve this constraint is detailed by *Bennett et al.* [1996]. The relative motions that we thus determine provide accurate boundary conditions on the rates of strain accumulating within the northern Basin and Range areas bounded by the CP, CGB, and SNGV blocks. We explore the strain fields in these bounded deforming areas in the next section.

[42] As discussed above, we make the approximation that relative motions among these regions are adequately represented by rigid body translations with no net rotation. Strain in the zones separating these rigid domains is investigated in the next section. We ignore spillover of elastic strain from these boundary zones. Translation results are virtually unaffected by these strains. We made no attempt to model transient deformations associated with past large earth-

quakes. Our weighted least squares estimates thus represent the average motions of the subsets of velocity estimates defining the CP, CGB, and SNGV regions.

[43] Figure 9 summarizes our block motion estimates, with a comparison to other recent studies based on analyses of GPS data [*Gan et al.*, 2000; *Dixon et al.*, 2000], and deformation modeling [*Hearn and Humphreys*, 1998], and Table 5 lists our estimates. In comparing our SNGV-CP relative motion estimate of 11.4 ± 0.3 mm yr^{-1} oriented N47° ± 1°W with the SNGV-NA estimates of these other studies we included the small 0.9 mm yr^{-1} CP-NA motion determined above. This yields an estimate for SNGV-NA velocity of 12.3 mm yr^{-1} oriented N47°W, consistent with the direct estimate of 12.4 mm yr^{-1} oriented N47°W (see above) and in general agreement with the directions of the SNGV-NA estimates of *Dixon et al.* [2000] and *Hearn and Humphreys* [1998]. This direction is more westerly than the directions of Pacific–North America relative plate motion [*DeMets and Dixon*, 1999] and the trace of the San Andreas fault system in the latitude band of ~36°–38°N. Because the SNGV-NA motion is more westerly than the trace of the San Andreas fault and the direction of P-NA relative plate motion, it implies a small amount of shortening perpendicular to the trace of the fault to the west (see below), consistent with inferences based on local studies of deformation in and around the Coast Ranges [e.g., *Freymueller et al.*, 1999; *Unruh and Lettis*, 1998; *Prescott et al.*, 2001].

[44] Residual velocities after estimating and removing the relative block motions are shown in Figure 11. The NRMS values for the CP, CGB, and SNGV regions using this model are 0.7, 0.9, and 1.6, respectively. The WRMS values are 0.3, 0.6, and 1.3 mm yr^{-1}, respectively. These values are identical to those calculated above on a block by block basis, indicating that the GPS data are amenable to the velocity vector closure constraint used for the present calculation.

[45] Our SNGV-NA estimate is slightly slower than these other recent estimates (Figure 9). As we demonstrated in the previous section, this is due to the increased number of sites that we have used to define the SNGV microplate and to differences between realizations of the NA fixed reference frame. Also mentioned above, an important consideration in assessing the significance of the relative motion estimates between plate boundary blocks and NA is an investigation of the nature of errors underlying the NA frame determination, which is beyond the scope of this paper. Our strain rate analyses below, however, depend only on the relative motions between blocks within the plate boundary zone and not on their motions with respect to the continental interior.

[46] Our CGB-CP estimate, which represents the integrated deformation across the eastern Great Basin, is 2.8 ± 0.2 mm yr^{-1}, N84° ± 5°W. This estimate is slower than previous estimates for EGB extension based on the 5 ± 1 mm yr^{-1} roughly west directed velocity estimate for VLBI site ELY (located near GPS sites EGANCGPS, E2ZZNBAR, and ELYASNGV) with respect to NA [e.g., *Dixon et al.*, 1995] but is consistent with more recent analyses based on GPS data and modeling (e.g., Figure 9) and the combined space geodetic velocity solution of *Bennett et al.* [2002], which yields an estimate for ELY of 2.9 ± 0.7 mm yr^{-1}. The westerly direction of this motion is consistent with the regional direction of eastern Great Basin spreading as indicated by the northerly orientation of Basin and Range topography and associated normal faulting (Figure 1a).

[47] Our SNGV-CGB estimate records a displacement rate accommodated across the western Great Basin region of 9.3 ± 0.2 mm yr^{-1}, N37° ± 2°W. Although this rate is in the range of previously reported estimates for the total rate of deformation across the ECSZ through the Mojave Desert to the south (latitude ~35°N) of 6–12 mm yr^{-1} [e.g., *Savage et al.*, 1990; *Sauber et al.*, 1994], it is generally much slower than recent estimates across the shear zone near Death Valley (latitude ~37°N) of 13 mm yr^{-1} [*Miller et al.*, 2001] and 11.1 ± 0.3 mm yr^{-1} [*McClusky et al.*, 2001] (also see Figure 9). However, our slower estimate better explains paleoseismological estimates for slip rate across the right lateral faults of the shear zone at the latitude of Death Valley, which include the Death Valley–Furnace Creek fault zone (DVFC), the Hunter Mountain–Panamint Valley fault zone (HMPV), and the Owens Valley fault zone (OWFZ) (Figure 1a), which sum to at most ~9 mm yr^{-1} [see *Hearn and Humphreys*, 1998, Table 1; *Lee et al.*, 2001]. The orientation of our SNGV-CGB relative motion estimate is very close to the direction of Pacific–North America relative plate motion.

2.7. Strain Rate Analyses

[48] On the basis of the large-scale kinematic analyses above, the plate boundary zone in the southwestern United States appears to be divisible into a relatively small number of geodetically defined provinces (Figure 10), whose boundaries do not necessarily coincide with those of tectonic elements defined on the basis of seismicity, Quaternary faulting, geomorphology, or other criteria (e.g., Figure 1b). These provinces include the CP, CGB, and SNGV provinces, which, as discussed above, are relatively rigid. These blocks bound more rapidly deforming provinces, including the San Andreas fault zone (SAFZ), eastern Great Basin (EGB), and western Great Basin (WGB) provinces. The EGB province corresponds to the region between the CP and the CGB and is so named because it is almost wholly contained within the eastern part of the Great Basin physiographic province. The WGB province lies between the SNGV and the CGB and is bordered on its southern extremity by the SAFZ province. It is so named because its southern and western boundaries also coincide with the physiographic limits of the Great Basin (Figure 10). Owing to a lack of geodetic data, the northern boundaries of these provinces are as yet not defined.

[49] Relative motion estimates for the CP, CGB, and SNGV regions provide precise boundary conditions on the directions and rates of integrated deformation within the EGB and WGB provinces, thereby constraining the rates and styles of deformation within the northern Basin and Range. In this section we investigate the pattern of strain

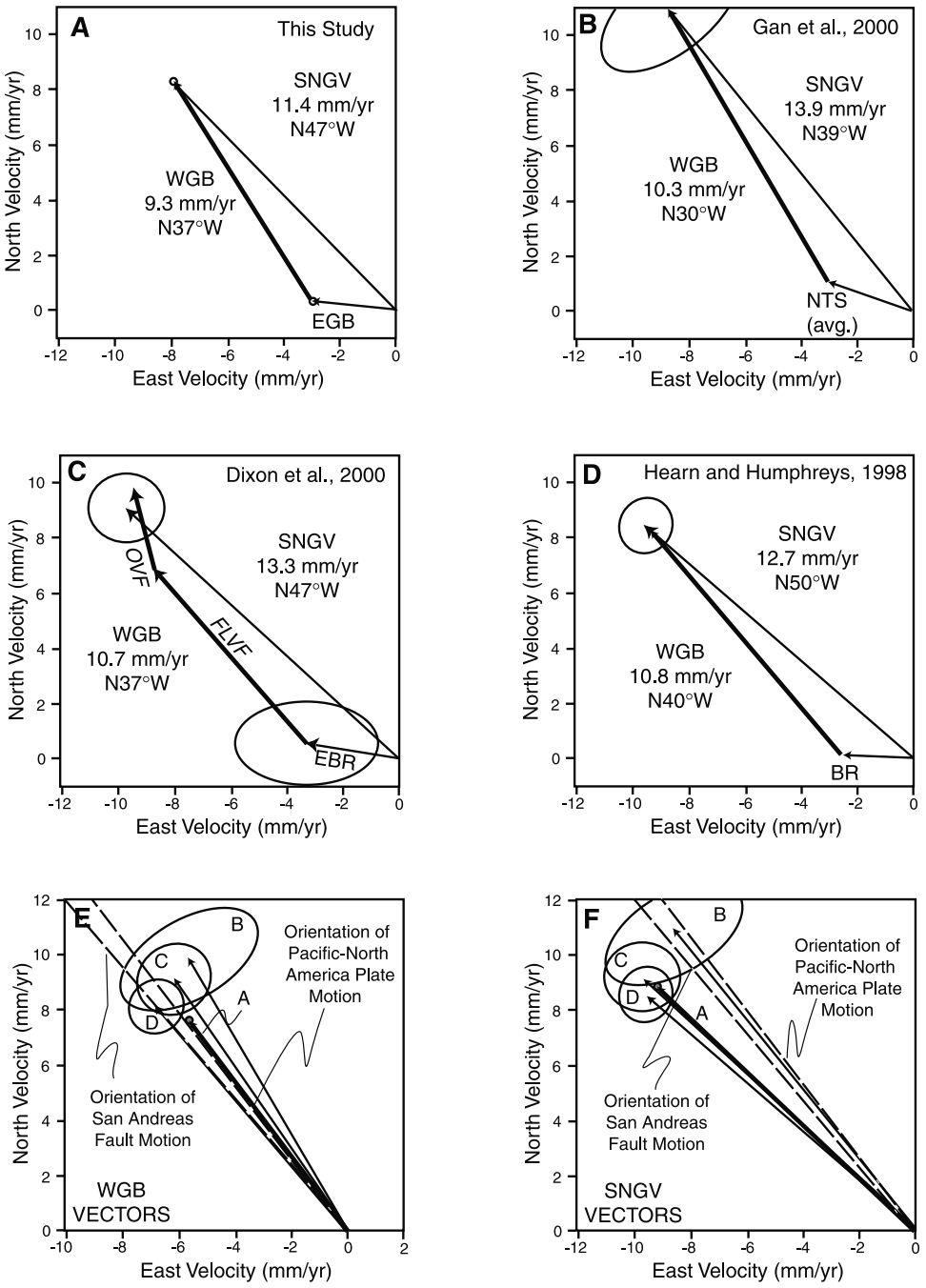

Figure 9. Comparison of velocity vector diagrams summarizing the kinematics of crustal deformation in the northern Basin and Range: (a) this study, rates with respect to the CP microplate, (b) *Gan et al.* [2000], rates with respect to the NA, (c) *Dixon et al.* [2000], rates with respect to the NA, and (d) *Hearn and Humphreys* [1998], rates with respect to the NA. (e) A comparison between estimates for total deformation accommodated across the western Great Basin (WGB). (f) A comparison between estimates for Sierra Nevada–Great Valley (SNGV) microplate motion with respect to North America. Error ellipses represent the 95% confidence level. NTS (avg.) is the average velocity among GPS stations from *Gan et al.* [2000] sites at the Nevada Test Site; EBR is the eastern Basin and Range based on GPS data from *Dixon et al.* [2000]; and BR is the Basin and Range boundary condition estimated by *Hearn and Humphreys* [1998].

Table 5. Relative Microplate Translations[a]

Microplate	Rate, mm yr^{-1}	Azimuth, deg
CGB-CP	2.8 ± 0.2	N84° ± 5°W
SNGV−CGB	9.3 ± 0.2	N37° ± 2°W
SNGV−CP	11.4 ± 0.3	N47° ± 1°W

[a]Subject to closure fitting constraints (see text).

accumulation given these boundary conditions and the GPS velocity estimates within these regions.

[50] Toward this end, we formed four subsets of velocity estimates to define four strain domains (Table 1). These domains represent the EGB province as defined above and three subdomains within the WGB province (Table 1). We resolved each subset of site velocity estimates into components parallel and perpendicular to kinematic axes defined by the boundary conditions derived in the previous section. We then fit planes through each of the resulting horizontal components of the velocity estimates, modeling the velocity gradient field as a constant in space within each of these domains. Thus, for each site we have a pair of equations of the form

$$v_i = \sum_{j=1}^{2} \dot{\varepsilon}_{ij} x_j + c_i, \tag{1}$$

where v_i is the ith component of velocity at that site, $\dot{\varepsilon}_{ij}$ is the ijth component of the horizontal velocity gradient tensor, x_j is the distance of the site measured from a local Cartesian referencein the jth direction, and c_i is a constant.

[51] We did not force the model deformation fields within each domain to match those of neighboring domains along common boundaries as is commonly done in strain rate field

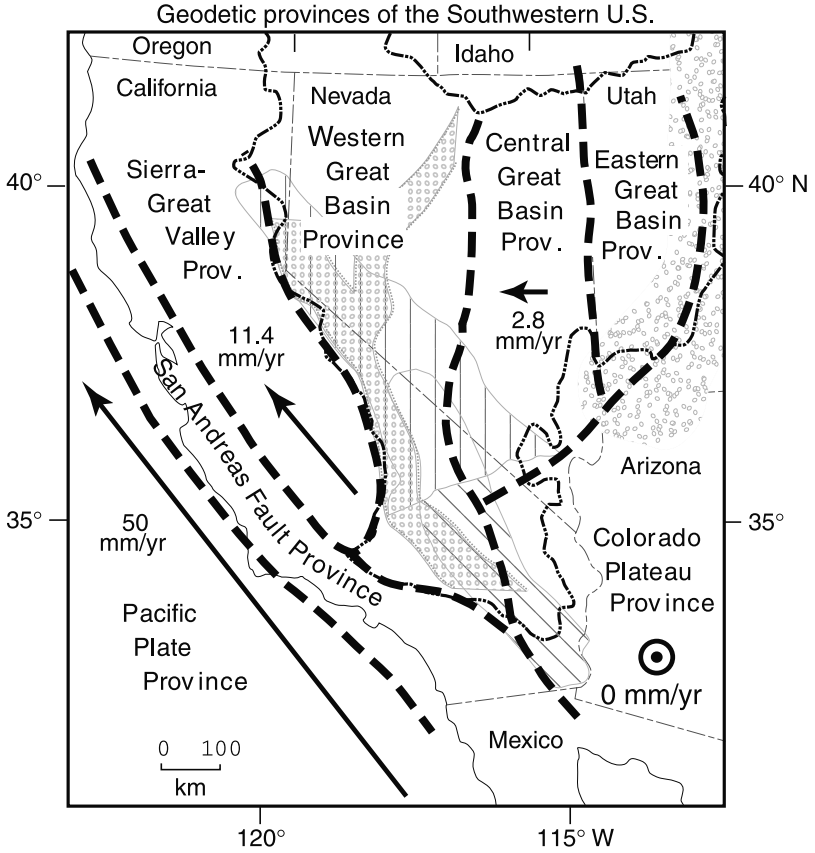

Figure 10. Geodetically determined strain provinces of the southwestern United States. Pattern filled regions show tectonic elements as in Figure 1b. Velocity vectors shown for the central Great Basin (CGB) and Sierra Nevada–Great Valley (SNGV) regions with respect to the Colorado Plateau (CP) fixed reference frame were determined from a block-strain model fit to the velocity data of Figure 2 (see text). CGB-CP relative motion of 2.8 mm yr^{-1} N84°W is accommodated in part by diffuse deformation across the eastern Great Basin (EGB) province, whereas SNGV-CGB relative motion of 9.3 mm yr^{-1} N37°W is accommodated in part by diffuse deformation across the western Great Basin (WGB) province. Rapid deformation in relatively narrow bands along the edges of the Great Basin also accommodates some of the relative motions. The broadening of the WGB region from south to north results in shear zone parallel extension within the WGB region, which appears to be accommodated across the central Nevada seismic belt.

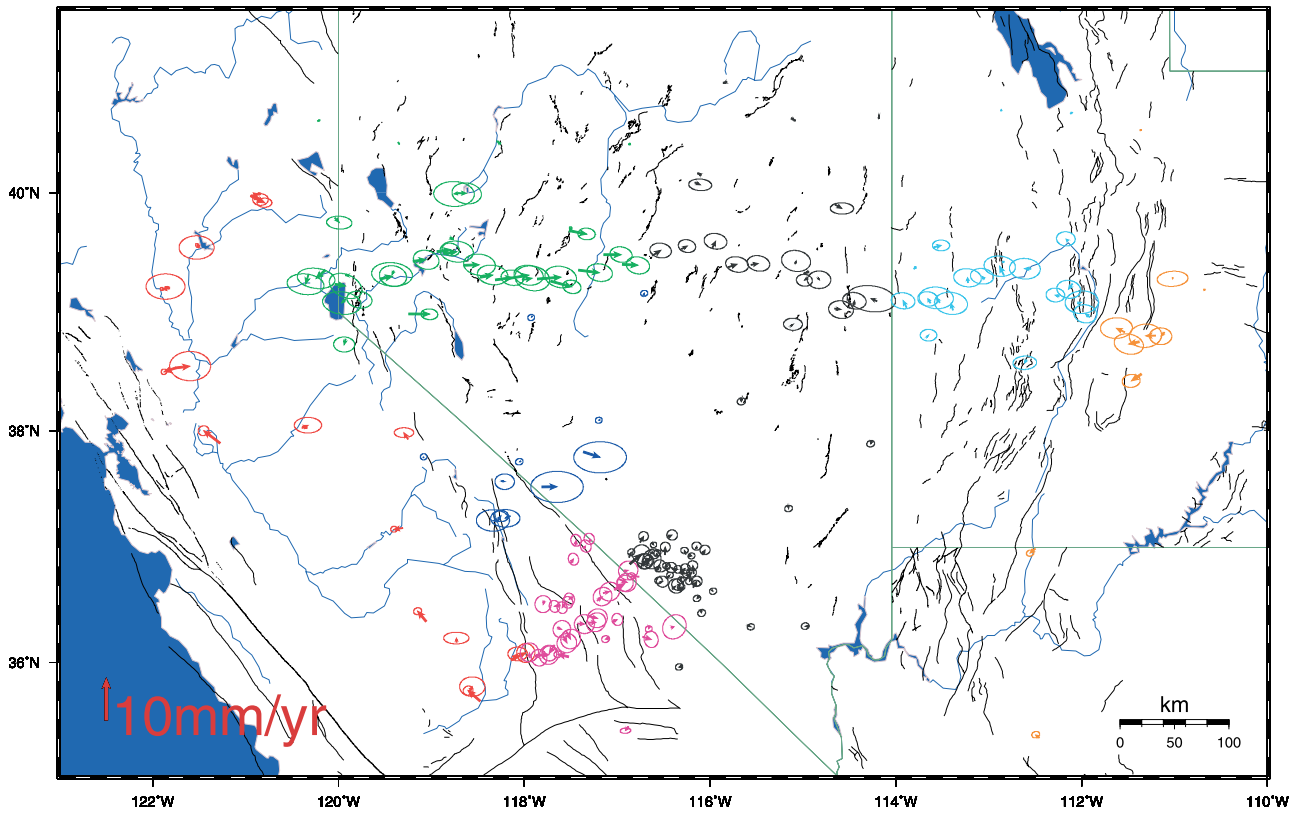

Figure 11. Residual velocities after removing the block-strain model depicted in Figure 10. Error ellipses represent the 95% confidence level. The results are shown in a no-net translation reference frame. Red, Sierra Nevada–Great Valley (SNGV) region; green, northwestern Great Basin (NWGB) region; dark blue, west central Great Basin (CWGB) region; purple, southwestern Great Basin (SWGB) region; black, central Great Basin region (CGB); light blue, eastern Great Basin (EGB) region; and orange, Colorado Plateau (CP). Residual velocities associated with several of the long operating CGPS sites in the northern Basin and Range are difficult to see because they are so small relative to the significantly noisier campaign data sets. Residual rates for these stations are typically less than 0.5 mm yr^{-1}. The NRMS of the overall fit of the block strain model to all of these stations is 1.0.

estimations. Rather, our model velocity field is allowed to be discontinuous at the domain boundaries. We chose to do this for two reasons. First, domain boundaries are not well defined by the data themselves because of the limited density of stations. If we were to specify subjectively exact boundaries and force velocity field continuity along these boundaries, we could potentially introduce significant biases in the resulting strain fields. Second, by allowing the boundaries to be free of constraints the model is better able to accommodate rapid strains at block boundaries. Large strains over short distances would otherwise not be resolved with the simple course discretization that we have chosen, requiring either a more flexible model [e.g., *Haines and Holt*, 1993] or successive subdivisions and refinements of the model [e.g., *Crespi and Riguzzi*, 2000]. However, such refinements would largely defeat one of our main objectives, a low-order reduction of the large-scale pattern of plate boundary zone deformation, which we are seeking to achieve by restricting the number of distinct deformation domains in our model.

[52] The velocity gradients that we estimated using this model are listed in Table 4. Figure 11 shows the residual velocities after removing the model from the GPS data. We also present the strain results in two dimensions by obliquely projecting both data and model values in the plane to account for variations in the velocity components as a function of distance orthogonal to the abscissas of the plots. In other words, each two-dimensional plot shows a profile obliquely "looking" parallel to the best fit plane, as opposed to simple projections of velocity components onto a vertical plane. To investigate shear, for example, we "correct" the data by plotting the points

$$v_i - \hat{\dot{\varepsilon}}_{ii} x_i \tag{2}$$

and the strain model by plotting the function of x_j

$$\hat{\dot{\varepsilon}}_{ij} x_j + \hat{c}_i, \tag{3}$$

where $\hat{\dot{\varepsilon}}_{ii}$, $\hat{\dot{\varepsilon}}_{ij}$, and $\hat{c}_i$ are the parameter estimates that we determined from the GPS site velocity estimate subsets.

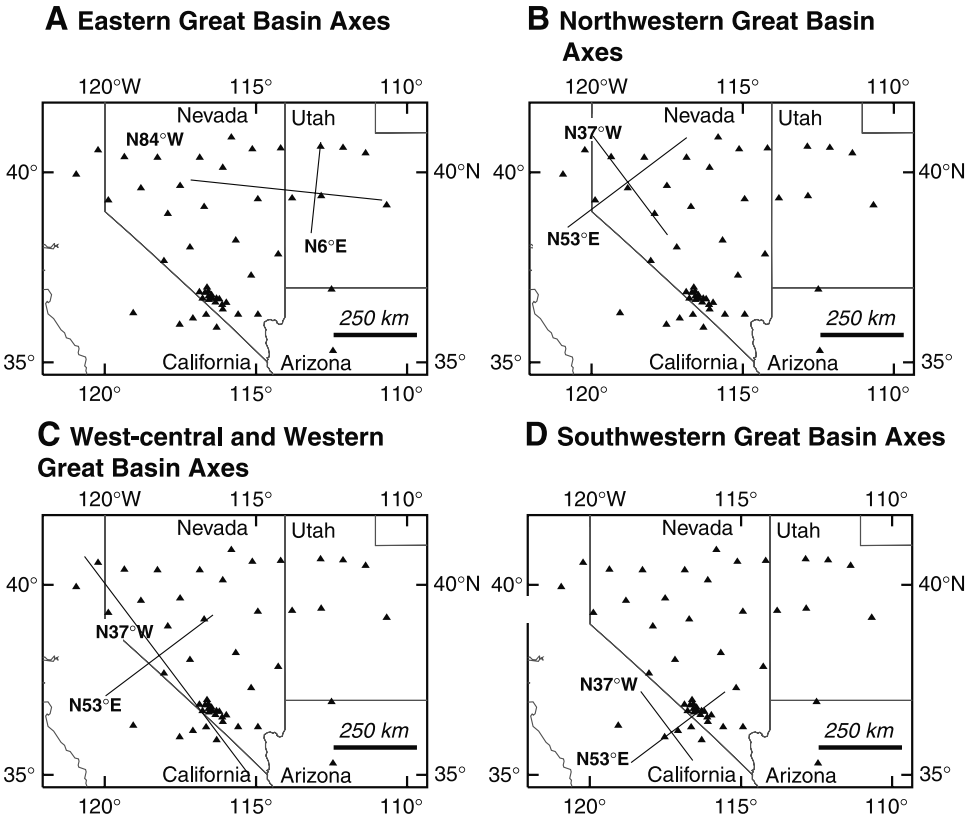

Figure 12. Maps showing the location and orientation of the coordinate axes used for strain analyses in each of the four strain domains (see the text for definitions of the strain domains). The coordinate systems were determined by the velocity vectors of Figure 9a. The origin of the axes is the centroid of the GPS subnetworks that were used to define the strain domains.

To investigate extension and shortening, we similarly correct the data by plotting the points

$$v_i - \hat{\dot{\varepsilon}}_{ij} x_j \tag{4}$$

and the model by plotting the function of x_i

$$\hat{\dot{\varepsilon}}_{ii} x_i + \hat{c}_i. \tag{5}$$

The locations of these profiles are shown in Figure 12.

2.8. Eastern Great Basin

[53] Geologically the eastern Great Basin is characterized by a complex system of north trending normal faults that bound north trending mountain ranges spaced about 30 km apart. The Wasatch fault zone defines the eastern boundary of this region near the latitude of 40°N. How this system of normal faults relates to the greater Pacific–North America plate boundary zone remains poorly understood.

[54] A total of 21 GPS velocity estimates (Table 1) constrains the velocity gradient field of the EGB domain (Table 4). Figure 13 shows the N84°W components of these velocities as a function of N84°W distance, corrected using equations (4) and (5) for the small net variation in the N6°E direction. The NRMS of the fit to these data is 0.4, and the WRMS misfit is 0.2 mm yr^{-1}. The resulting velocity gradient tensor estimates indicate 7 ± 3 nstr yr^{-1} east-west extension within this region, but as Figure 13 illustrates, significantly more rapid deformation is apparent across a comparatively narrow zone near the Wasatch fault zone between our CP and EGB domains. A linear regression through several (corrected) data points of Figure 13 in a ~160 km wide zone located immediately west of the Wasatch fault provides an estimate of 20 ± 1 nstr yr^{-1} for the rate of strain accumulation near this fault [*Friedrich et al.*, 2003]. However, the rate that we obtain for this narrow region depends strongly on the width over which the slope was estimated, with higher strain rates when averaging over shorter distances and lower strain rates when averaging over longer distances.

2.9. Western Great Basin

[55] A number of previous terrestrial and space geodetic investigations pertain to the distribution of strain within the WGB province [e.g., *Savage et al.*, 1990, 1995; *Dixon et al.*, 1995; *Bennett et al.*, 1997, 1998; *Gan et al.*, 2000; *Dixon et al.*, 2000; *Oldow et al.*, 2001; *McClusky et al.*, 2001; *Miller et al.*, 2001]. No one of these previous studies, however, has had the aperture and resolution necessary to

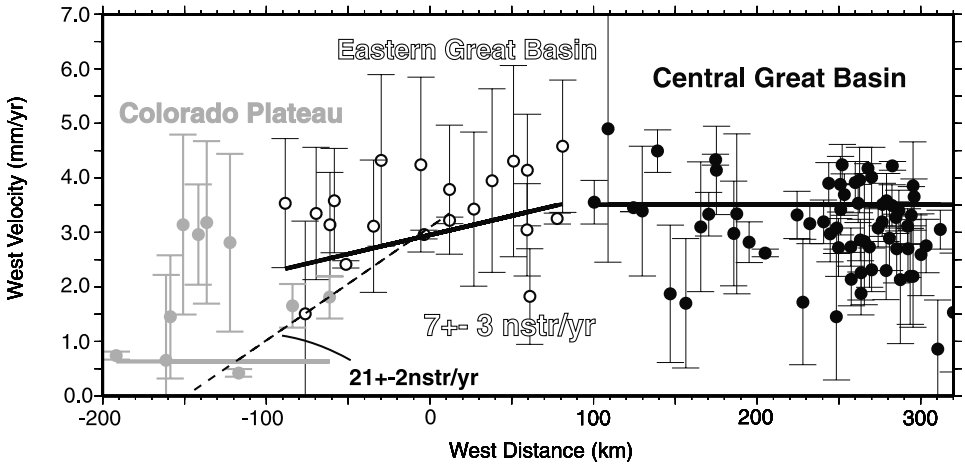

Figure 13. West components of velocity as a function of west distance for the Colorado Plateau (CP; gray circles), eastern Great Basin (EGB; open circles), and central Great Basin (CGB; solid circles) domains. Velocities refer to the North America reference frame. Error bars represent 1 standard deviation. Both data and model have been corrected using equations (4) and (5). The solid lines drawn over the data show the block-strain model. Zero slope lines indicate that the CP and CGB regions are not internally deforming in the model. The slope of the dashed line provides an estimate for the extension rate across a ~160 km wide zone in the vicinity of the Wasatch fault zone. The strain rate across the Wasatch region is very sensitive to the width of this region.

address the details of the entire strain field. Both the internal strain field and how it relates to Pacific–North America relative plate motion and crustal spreading in the eastern Great Basin is therefore not yet well understood.

[56] We estimated velocity gradients throughout the region bounded by the CGB and SNGV blocks using equation (1) and the velocity estimates for various subsets of sites spanning the region (Table 1). As we discussed above, we allowed for strain rate variation within this strain domain by separating it into northern, central, and southern subdomains. We used the GPS velocity estimates for sites in each domain to estimate the horizontal strain rate tensor for each domain separately. The northern and southern domains are each defined by 33 velocities, whereas the central domain is defined by 11 velocities. We did not use sites from *Gan et al.* [2000] or IGS in the vicinity of the Coso geothermal region because this region experiences rapid nontectonic motions [*Fialko and Simons*, 2001b; *Wicks et al.*, 2001].

[57] We estimated velocity gradients following the procedure outlined above, using SNGV-CGB relative motion to determine the kinematic axes for calculation of strain rates. Figure 14a shows variations in the N37°W components of velocity with N53°E distance. The NRMSs of the fit of the velocity gradient model to these velocity data for the northern, central, and southern domains are 1.1, 0.3, and 0.6, respectively. The WRMS scatter about these fits for these domains are 0.5, 0.4, and 0.7 mm yr^{-1}, respectively. Both the data and model of Figure 14a have been corrected using equations (2) and (3) for the net variation in the N37°W velocity component as a function of distance in the direction N37°W (Table 4).

[58] Right lateral shear strain is apparent in Figure 14a with rate estimates of 57 ± 9 nstr yr^{-1} for the southern domain, 25 ± 6 nstr yr^{-1} in the central domain, and 36 ± 1 nstr yr^{-1} in the northern domain. Shear strain appears to be accumulating more or less uniformly across the shear zone in the northern and southern domains. Because the total deformation across the WGB region is 9.3 ± 0.2 mm yr^{-1} for both these domains, the shear zone correspondingly increases in width, from ~125 km across the southern domain to ~300 km across the northern domain. Shear strain is less uniform across the central domain, as is evidenced by the relatively low rate across the interior of the domain and the ~4.5 mm yr^{-1} jump coincident with its boundary with the SNGV domains. This implies that rapid shear is concentrated in a fairly narrow band along the eastern margin of the Sierra Nevada.

[59] Several previous investigations have reported rates within the Walker Lane belt. Previously reported rates and directions of strain accumulation are fairly consistent for the northern strain domain but vary considerably for the southern domain. Within the northern domain, *Savage et al.* [1995] reported a rate of 33 ± 3 nstr yr^{-1} right lateral shear in the vicinity of the central Nevada seismic zone across planes oriented N15 ± 3°W. On the basis of linear regression of the north components of motion, *Bennett et al.* [1998] reported an average rate of 26 ± 5 nstr yr^{-1} right lateral shear on planes oriented due north across the region. The strain rate that we report here, which is resolved onto planes oriented N37°W is similar to both of these previous estimates in magnitude.

[60] Strain rates for the central WGB domain are less well constrained geodetically. *Oldow et al.* [2001] used GPS measurements to infer that deformation across the region was not entirely concentrated at the Sierran front but rather distributed across a broad region. Our solution using these

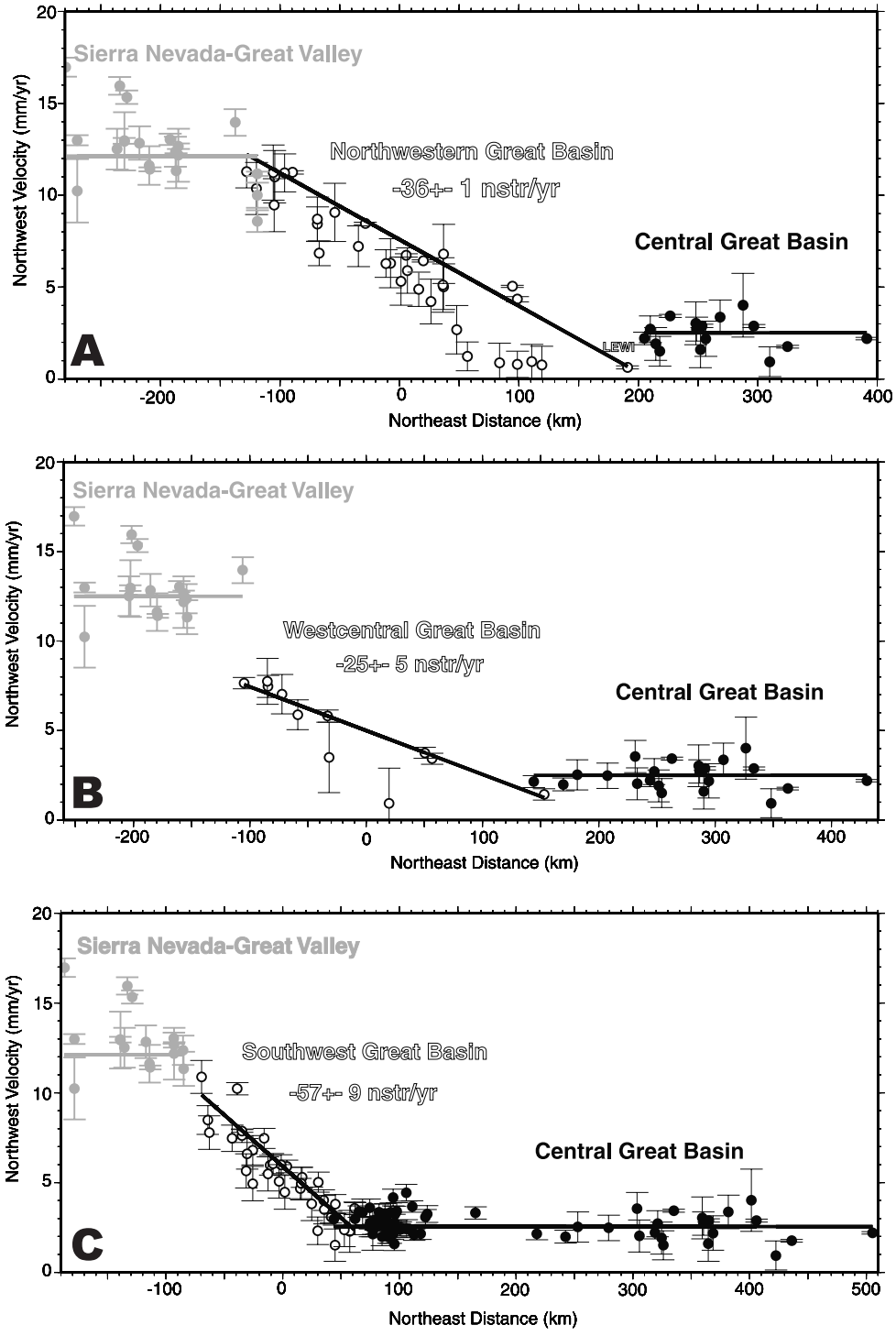

Figure 14. (a) N37°W components of velocity as a function of N53°E distance for the Sierra Nevada–Great Valley (SNGV; gray circles), northwestern Great Basin (NWGB; open circles), and central Great Basin (CGB; solid circles) domains. Velocities refer to the North America reference frame. Error bars represent 1 standard deviation. Both data and model have been corrected using equations (2) and (3). The lines show the block-strain model. Zero slope indicates that the SNGV and CGB regions are not internally deforming in the model. Site LEWICGPS in the northwest Great Basin domain is labeled. (b) Same as for Figure 14a but for west central Great Basin domain (CWGB). (c) Same as for Figure 14a but for southwestern Great Basin domain (SWGB).

data, shown in Figures 14a and 14b, also indicates concentrated strain along the eastern Sierra front, with slower, but nevertheless significant, strain well east of the Sierras into the Walker Lane belt.

[61] For the southern domain, *Gan et al.* [2000] reported an average shear zone rate of 39 ± 4 nstr yr^{-1} right lateral shear across planes oriented N23°W, whereas *Savage and Lisowski* [1995] reported a rate of 58 ± 7 nstr yr^{-1} right lateral shear in the vicinity of the Owens Valley fault zone across planes oriented N18°W. Our estimate of 57 ± 9 nstr yr^{-1} is in agreement at the 2σ level with both of these previous estimates. Differences are perhaps a reflection of the differing apertures of the networks used to infer the strain rates, which range from the ~10–100 km scale of individual faults to the plate boundary zone scale of >1000 km, and possible local effects in the vicinity of the Owens Valley fault zone such as postseismic strain associated with the 1872 Owens Valley earthquake [e.g., *Dixon et al.*, 2000] or deformation associated with the Coso geothermal field [*Fialko and Simons*, 2001b; *Wicks et al.*, 2001].

[62] At the latitude of Death Valley, uniform strain accumulation implies roughly equal amounts (~3 mm yr^{-1}) of strike slip motion along the Death Valley–Furnace Creek, Hunter Mountain–Panamint Valley, and Owens Valley Fault zones, in general agreement with paleoseismological inferences [*Beanland and Clark*, 1995; *Butler et al.*, 1988; *Reheis and Sawyer*, 1997; *Burchfiel et al.*, 1987; *Zhang et al.*, 1990; *Lee et al.*, 2001]. Previous geodetic and modeling studies, in contrast, have concentrated slip in either the east or west portion of the shear zone. For example, our inference for the slip rate of the Death Valley–Furnace Creek fault of ~3 mm yr^{-1} is only about half that inferred by *Hearn and Humphreys* [1998]. Our estimates of ~3 mm yr^{-1} slip rate for each of the Death Valley–Furnace Creek and Hunter Mountain–Panamint Valley fault zones are consistent, however, with previous estimates based on simple elastic fault models [*Bennett et al.*, 1997; *Gan et al.*, 2000]. Our estimate of ~3 mm yr^{-1} for the Owens Valley fault slip rate is only about half that of previous geodetic estimates [*Savage and Lisowski*, 1995; *Gan et al.*, 2000]. However, our estimate for this fault zone is in agreement with the kinematic modeling of *Hearn and Humphreys* [1998] and is supported by recent paleoseismological investigations of the Owens Valley fault zone, suggesting the Holocene slip rate is between 1.5 and 3.8 mm yr^{-1}. One difference between our estimates and some previous geodetic estimates for slip rate on the Owens Valley fault system is that our rate is based, in part, on constraints from far field stations in the Basin and Range province and the Sierra Nevada–Great Valley microplate, which tightly constrain total deformation across the shear zone. It is possible that narrow aperture geodetic arrays, which are confined to the shear zone, are more sensitive to possible postseismic relaxation associated with the 1872 *M*8 Owens Valley earthquake than our larger aperture study. *Dixon et al.* [2000] has shown, for example, that differences between the paleoseismological slip rate estimates of ~2–3 mm yr^{-1} [e.g., *Beanland and Clark*, 1995] and previous geodetic slip rate estimates of up to 3 times this rate can be reconciled by accounting for such effects for some networks.

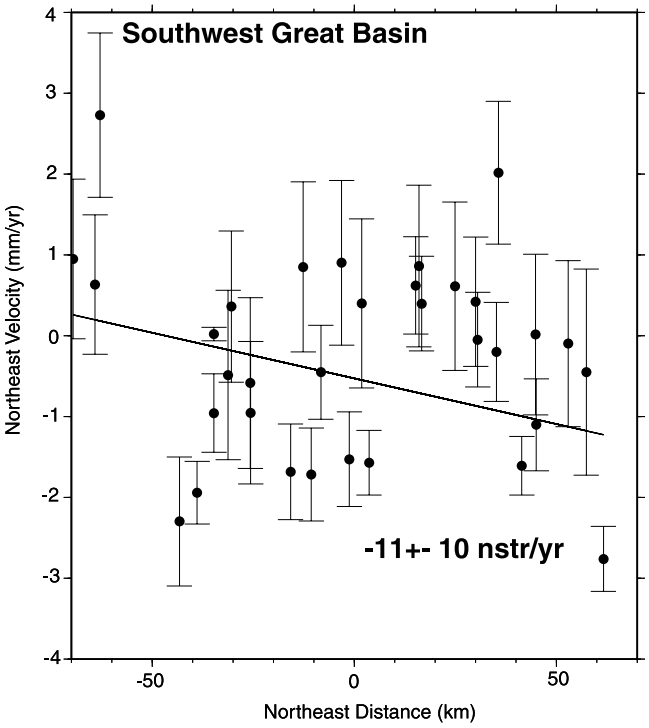

Figure 15. N53°E components of velocity as a function of N53°E distance for the southwestern great Basin (SWGB) domain. Velocities refer to the North America reference frame. Error bars represent 1 standard deviation. The sloped line represents the block-strain model for this region. Shortening across the region is only marginally significant. There is a slight hint of nonlinear velocity variation across the shear zone.

[63] Velocity variation in the N53°E direction is only marginally significant within central and southern domains (Table 4) as expected; by construction the block model allows no net variation in velocity in this direction. However, shortening in the N53°E direction is very significant within the northern domain. This shortening is compensated by a relatively narrow zone of rapid extension along the eastern Sierran front. Figure 15 illustrates the N53°E components of velocity across and within the WGB. The N53°E components of velocity are plotted as a function of N53°E distance, again corrected using equations (4) and (5) for the net variations in the N37°W direction. There is a hint in these data of a sinusoidally varying pattern of amplitude about 2 mm and wavelength of approximately 100 km, but significant improvements to the resolution of the GPS velocity field will be necessary in order to attribute confidently this pattern to tectonic deformation. We discuss these nonlinear deformation patterns in more detail below.

[64] The eastern boundary of the WGB province is not parallel to the shear direction within the shear zone, reflecting a large-scale "pull apart" geometry of the region. The northward widening requires a component of shear parallel

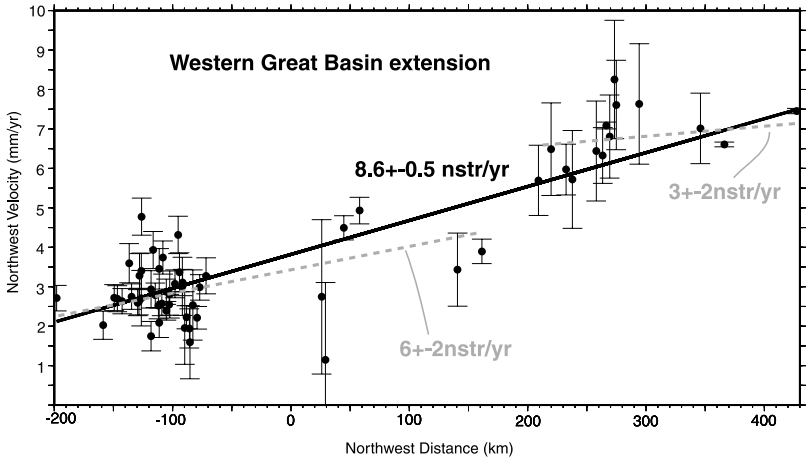

Figure 16. N37°W components of velocity as a function of N37°W distance in the western Great Basin (WGB). Velocities refer to the North America reference frame. Error bars represent 1 standard deviation. Both data and model have been corrected using equations (4) and (5). The solid black line shows the linear regression to the entire data set. The slope of this line provides an estimate for the average extension rate in the direction of the WGB shear of 8.6 ± 0.5 nstr yr^{-1}. The data are fit slightly better by allowing for a rapid zone of strain accumulation coincident with the central Nevada seismic belt (Figure 1b). The dashed lines show the best fit model that allows for a zone of rapid deformation. About 2 mm yr^{-1} appears to be accommodated across a zone of no wider than 50 km, indicating a minimum strain rate of about 40 nstr yr^{-1} across the CNSB region.

extension. Sites along or near the eastern boundary in the southern and central WGB and CGB domains, which do not move much with respect to the CGB frame (Figure 8), align approximately with the center of the shear zone in the north, which moves about 4.7 mm yr^{-1} with respect to this frame. To investigate the magnitude and distribution of this extension, we used 61 sites in a narrow, northwest elongate band just east of the California-Nevada border. This band of stations is narrow enough in the direction N53°E that differences in shear strain rates from south to north are negligible. Using a model of uniform strain within the domain defined by these sites, we observe an average extensional strain of 8.6 ± 0.5 nstr yr^{-1} in the direction of SNGV-CGB relative motion, comparable to the Basin and Range average of 10 nstr yr^{-1} [e.g., *Bennett et al.*, 1998], but implying a distinctly different mechanism from extension on north trending, range-bounding normal faults. The NRMS for this fit is 1.9. The WRMS scatter about the fit is 1.5 mm yr^{-1}. The data are fit slightly better by a model in which extensional strain is concentrated within the central Nevada seismic belt (Figures 1a and 1b). Using such a model, we estimate an extension rate of at least 40 nstr yr^{-1} over a distance of about 50 km or less (Figure 16). This strain rate estimate is a minimum because the sparse station coverage does not tightly constrain the width of the potentially rapidly straining region.

[65] The large-scale pull apart kinematics suggested by the GPS data are consistent with both geological and seismological patterns within the WGB. Crustal extension accommodated by right stepping right lateral faults on a much smaller scale is common within the shear zone [*Burchfiel and Stewart*, 1966; *Burchfiel et al.*, 1987]. Several northeast trending normal or detachment faults, such as the Deep Springs fault and the Silver Peak–Lone Mountain detachment system, which transfer northwest directed slip into the Basin and Range [e.g., *Oldow et al.*, 1994; *Reheis and Dixon*, 1996], are of the correct location, orientation, and slip sense to accommodate at least part of the observed extension across the inboard step of the shear zone. The pattern of seismic rupture over the last 150 years in the region also reflects this overall kinematics (Figure 1a). In the southern part of the province, ruptures including the 1872 Owens Valley, 1932 Cedar Mountain, 1992 Landers, and 1999 Hector Mine earthquakes have been predominantly right lateral strike slip faulting [*Sieh et al.*, 1993; *Beanland and Clark*, 1995; *Bell et al.*, 1999]. To the north, in the central Nevada seismic belt, the 1954 Rainbow Mountain–Fairview Peak–Dixie Valley earthquake sequence shows right oblique normal faulting, with a progressively greater amount of normal faulting from south to north [*Doser and Kanamori*, 1986; *Caskey et al.*, 1996]. The northernmost historic event in the belt, the 1915 Pleasant Valley earthquake, appears to have involved nearly pure normal faulting [*Wallace*, 1984b].

2.10. Anomalous Motions

[66] In addition to the linear trends just discussed, there are a few instances where site motions are anomalous with respect to our simple kinematic model. These anomalies may record more complicated deformation signals related to more localized crustal dynamic phenomena. Throughout the remainder of this section we describe the larger of these anomalies, proceeding generally from east to west and north

to south, with reference to the simple kinematic model that we have constructed above. We leave more detailed investigations of these motions to future work.

[67] As observed by *Wernicke et al.* [2000], site LEWICGPS exhibits an anomalously slow velocity relative to neighboring sites in the CGB region (Figure 14a). This site is consistent with the simple model for site velocities in the NWGB region. These results imply that a narrow zone of fairly rapid shortening lies between the CGB and NWGB domains, a region where the geology indicates crustal extension accommodated by Holocene normal faulting. *Wernicke et al.* [2000] showed that relaxation effects associated with large Basin and Range earthquakes, such as the 1915 *M*7.3 Pleasant Valley earthquake, is a viable explanation for this anomalous motion. N53°E extension of 9 ± 2 nstr yr^{-1} across the NWGB domain (Table 4) is similarly compensated by a narrow zone of shortening along the boundary between the SNGV and NWGB regions. It is possible that this pattern of deformation reflects the same relaxation processes observed near site LEWICGPS.

[68] Within the shear zone at the latitude of Death Valley we also observe a hint of an anomalous sinusoidal pattern in the N53°E velocity components of amplitude ~2 mm yr^{-1} and wavelength of ~100 km in the components of site velocity perpendicular to the shear zone (Figure 15). *Bennett et al.* [1999] reported on a similar pattern, although of larger amplitude, observed along a profile just to the south of Figure 15. From the CGB on the east to the SNGV microplate on the west the deformation pattern changes from a zone of shortening, within and east of the northern Death Valley fault region, to a zone of extension to the west. We obviously cannot confidently attribute this pattern to a deformation signal without significant further study. The present level of uncertainties and station density in this region also pose a limitation. However, postseismic relaxation following the 1872 Owens Valley earthquake [e.g., *Malservisi et al.*, 2001], which involved ~1 m of normal slip [*Beanland and Clark*, 1995], could potentially provide a model to explain this pattern as more data are collected and this pattern comes more sharply into focus.

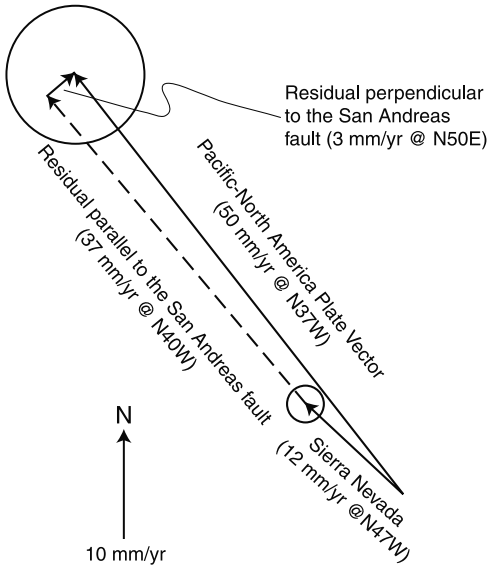

Figure 17. Velocity vector diagram illustrating the kinematics of Pacific–North America (P-NA) plate boundary deformation with estimates for the amount of deformation accommodated along the northern San Andreas fault system. The P-NA plate vector is from *DeMets and Dixon* [1999]. The Sierra Nevada velocity estimate is from this study.

3. Kinematics of Pacific–North America-Juan de Fuca Plate Interactions

[69] Our kinematic model for the northern Basin and Range has implications for the broader P-NA plate boundary. Figure 17 shows the plate circuit for the plate boundary zone, using the combined pole of P-NA relative plate motion of *DeMets and Dixon* [1999] (50.5°N, 248.2°E, 0.776° My^{-1}) evaluated at 37°N, 121.75°W (which is the longitude of the San Andreas fault at 37°N latitude). By decomposing the difference between our estimate for SNGV-NA motion and the P-NA vector into components parallel and perpendicular to the trace of the San Andreas fault (~320°) we estimate that the San Andreas transform system accommodates about 37 ± 2 mm yr^{-1}, consistent with the rate of 40 ± 1 mm yr^{-1} reported by *Freymueller et al.* [1999], which is based on observations from a fault-crossing network of GPS stations in northern California. We also constrain the rate of shortening perpendicular to the trace of the San Andreas fault system to be 3 ± 2 mm yr^{-1}, consistent with local GPS measurements [e.g., *Freymueller et al.*, 1999; *Prescott et al.*, 2001], kinematic studies based on VLBI observations [e.g., *Argus and Gordon*, 1991], and the late Cenozoic geologic record and seismogenic strain field east of the Hayward fault [e.g., *Unruh and Lettis*, 1998], and estimates inferred from regional kinematic models of the plate boundary zone [e.g., *Hearn and Humphreys*, 1998; *Dixon et al.*, 2000].

[70] As pointed out by *Pezzopane and Weldon* [1993], the orientation and magnitude of deformation within the northern Basin and Range also have implications for the direction and magnitude of convergence between the Juan de Fuca (JdF) and NA plates near the trench. Deformation within the overriding NA plate may account for the oblique component of convergence between these plates. How this deformation is accommodated within the plate north of latitude 40°N, however, is at present poorly constrained. On the basis of Neogene deformation, paleomagnetic rotations, and geodetic measurements, *Wells et al.* [1998] and *Savage et al.* [2000] infer 11–14 mm yr^{-1} N10°W motion of the Oregon coast with respect to North America, accommodated by a combination of Cascadia forearc rotation and translation or shear farther to the east. Figure 18 shows an estimate for the convergence between western Oregon (WOR) and the JdF plate assuming that SNGV-NA relative motion continues to the northwest, remaining east of the Juan de Fuca trench.

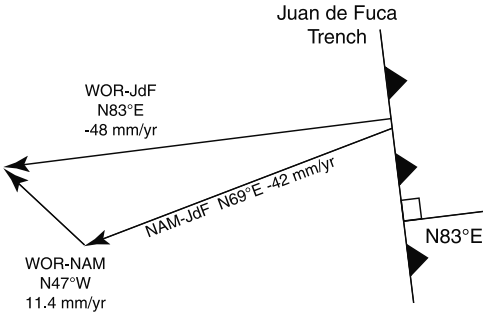

Figure 18. Velocity vector diagram showing hypothesized northwest continuation of northern Basin and Range deformation with implications for the subduction of the Juan de Fuca (JdF) plate. The relative motion between western Oregon (WOR) and North America (NA) assumes that Sierra Nevada–Great Valley (SNGV) microplate motion continues to the north, remaining east of the JdF trench. Under this scenario the relative motion between WOR and the JdF plate is more rapid than JdF-NA relative motion and is oriented perpendicular to the trench. The JdF-NA relative motion vector is from NUVEL-1.

This analysis suggests that the oblique component of JdF-WOR relative motion is essentially eliminated relative to JdF-NA motion estimates, while at the same time the rate of convergence between western Oregon and the JdF plate is increased by as much as 14%, or 6 mm yr^{-1}, relative to JdF-NA relative motion estimates.

4. Implications for Dynamics

[71] The Basin and Range province is a prime example of a diffuse plate boundary fault system, presenting one of the best opportunities to resolve the forces driving deformation. We consider three classes of driving forces: (1) those acting on the edges of the plates (plate boundary forces), (2) those acting on the base of the plates (basal forces), and (3) those internal to the lithosphere, such as buoyancy forces arising from density variations. A variety of models have been proposed to explain deformation within the Basin and Range province, all involving some combination of these [e.g., *Wernicke*, 1992; *Sonder and Jones*, 1999]. Although geodetic measurements can, in some instances, provide constraints on the rheology of the lithosphere, they do not bear directly on the force systems driving deformation. Contrasts in the styles of deformation can nevertheless provide important clues even in the absence of a complete understanding of stress-strain relations.

[72] The basic picture illustrated by our kinematic results distinguishes two distinct strain fields. The first involves east-west extension about the north striking, basin-bounding normal faults of the eastern part of the northern Basin and Range province. The lack of significant variation in N6°E motion in either the N84°W or N6°E directions (Table 4) in this region (i.e., uniaxial extension) carries with it the implication that east west extension is accompanied by vertical thinning. Anomalously thin crust and lithosphere have been inferred for this region from geophysical observations including seismic, gravity, topographic, and heat flow data sets [e.g., *Thompson and Burke*, 1974; *Lowry and Smith*, 1995].

[73] The second strain field involves northwest directed right lateral shear on a complex system of northwest striking right lateral strike slip faults, northeast striking left lateral strike slip faults, and north to northeast striking normal and detachment faults. The limited extent to which shear strain is observed to penetrate the continent is in accordance with simple viscous sheet models that predict that shear deformation would tend to be relatively localized along the edge of a shearing boundary [*England et al.*, 1985].

[74] To first order this pattern of strain accumulation is consistent with the pattern of faulting, which suggests a relatively uniform late Cenozoic stress field with pervasive horizontal minimum compressive stress oriented west to west-northwest [*Wright*, 1976]. In this model, maximum compressive stress would be oriented vertically in the EGB where normal faulting is prevalent and horizontally (directed northeast) within the WGB where strike slip faulting is prevalent. Plate boundary tractions alone may not account for this stress field. Contributions from both buoyancy forces and plate boundary tractions appear to be necessary [*Flesch et al.*, 2000].

[75] Second-order patterns of extension and shortening perpendicular to the predominant direction of shear are also difficult to reconcile with a model including only plate boundary tractions. These deformations would seem to indicate a complicated rheological structure for the WGB lithosphere and/or spatially variable forces acting within the lithosphere or along its base as might be provided by stresses associated with large earthquakes.

5. Conclusions

[76] Site velocities inferred from campaign and continuous GPS networks constrain the contemporary deformation field of the northern Basin and Range province. Geodetically identified provinces allow for an analysis of the strain rate field. The relative motions between relatively rigid provinces constrain the rate and style of deformation within deforming provinces.

[77] We identify three relatively undeforming blocks within the Pacific–North America plate boundary zone. These are the Colorado Plateau (CP), the central Great Basin (CGB), and the Sierra Nevada–Great Valley (SNGV) provinces. SNGV-CP relative motion is 11.4 ± 0.3 mm yr^{-1} oriented N47°W (Table 5), significantly more westerly than the directions of Pacific–North America relative plate motion and the trace of the San Andreas fault system. We also estimate SNGV-NA relative motion of 12.4 mm yr^{-1} oriented N47°W (Table 2). These results, together with the Pacific–North America relative plate motion model of *DeMets and Dixon* [1999], imply a right lateral slip rate of 37 ± 2 mm yr^{-1} for the San Andreas fault zone to the west, as well as 3 ± 2 mm yr^{-1} shortening orthogonal to the trace of the San Andreas fault.

[78] CGB CP relative motion of 2.8 ± 0.2 mm yr^{-1} oriented N84 ± 5°W (Table 5) is accommodated across the eastern great Basin (EGB) province. The EGB province is characterized by uniaxial east-west extension averaging 7 ± 3 nstr yr^{-1} (Table 4). More rapid extension is concentrated in a narrow zone in the vicinity of the Wasatch fault and neighboring faults to the west. The processes responsible for the observed extension likely involve crustal thinning.

[79] SNGV-CGB relative motion of 9.3 ± 0.2 mm yr^{-1} oriented N37 ± 3°W (Table 5) is accommodated across the western Great Basin (WGB) province. The WGB province is characterized by a complex strain field that is dominated by variable amounts of right lateral shear. The direction of shear is indistinguishable from the direction of Pacific–North America plate relative motion. Our estimate is slower than most previous geodetic estimates but is more consistent than these previous estimates with paleoseismological inferences for slip rates on faults within the southern WGB region. Right lateral shear strain is uniform in the southern and northern thirds of this region. In the central region, SNGV-CGB motion is accommodated by a combination of diffuse right lateral shear within the CWGB domain and more rapid shear within a narrow band along the eastern front of the Sierra Nevada.

[80] The large-scale pattern of deformation reveals two distinct strain fields. The first involves east-west extension about the north striking, basin-bounding normal faults of the eastern part of the northern Basin and Range province, and the second involves northwest directed right lateral shear on a complex system of northwest striking right lateral strike slip faults, northeast striking left lateral strike slip faults, and north to northeast striking normal and detachment faults. This pattern does not appear to be explained by dynamic models involving only plate boundary tractions [e.g., *England et al.*, 1985] but can be accounted for by a combination of plate boundary tractions and lithospheric buoyancy forces [e.g., *Flesch et al.*, 2000]. Localized anomalies with respect to this simple kinematic picture are also observed and may hold the key to understanding lithospheric dynamics within the plate boundary zone. Systematic variations in the components of site motion perpendicular to the WGB shear zone, for example, reveal strain signals not easily explained by dynamic models involving only plate boundary tractions. These strain anomalies may be related to postseismic relaxation associated with historic large earthquakes, but they could also be indicative of a complicated rheological structure for the lithosphere and/or other sources of spatially variable forces acting within the lithosphere or along its base.

[81] **Acknowledgments.** We made use of data from the BARD CGPS network operated by the University of California, Berkeley. We also made use of GPS data products provided by the SOPAC facility. We thank Timothy Dixon, Weijun Gan, and Wayne Thatcher for providing GPS velocity results and James Savage for details about some of the GPS campaign data. Parts of the figures were produced with the GMT software. We benefited from the comments and suggestions of Darrel Cowan, Tim Dixon, and an anonymous reviewer. This work was supported by DOE grants DE FC08-98NV 12081, NASA grant NAG5-8226, NSF grants EAR 94-18784 and EAR 97-25766, and USGS grant 99HQGR0212, California Institute of Technology, and the Smithsonian Institution.

References

Aoki, Y., P. Segall, T. Kato, P. Cervelli, and S. Shimada, Imaging magma transport during the 1997 seismic swarm off the Izu Peninsula, Japan, *Science*, *286*, 927–930, 1999.

Argus, D. F., and R. G. Gordon, Current Sierra-Nevada-North America plate motion from very long baseline interferometry: Implications for the kinematics of the western United States, *Geology*, *19*, 1085–1088, 1991.

Argus, D. F., and R. G. Gordon, Tests of the rigid-plate hypothesis and bounds on intraplate deformation using geodetic data from very long baseline interferometry, *J. Geophys. Res.*, *101*, 13,555–13,572, 1996.

Beanland, S., and M. M. Clark, The Owens Valley fault zone, eastern California, and surface rupture associated with the 1872 earthquake, *U.S. Geol. Surv. Bull.*, *1892*, 29 pp., 1995.

Bell, J., C. dePolo, A. Ramelli, A. Sarna-Wojcicki, and C. Meyer, Surface faulting and paleoseismic history of the 1932 Cedar Mountain earthquake area, west-central Nevada, and implications for modern tectonics of the Walker Lane, *Geol. Soc. Am. Bull.*, *90*, 3551–3557, 1999.

Bennett, R. A., W. Rodi, and R. E. Reilinger, Global Positioning System constraints on fault slip rates in southern California and northern Baja, Mexico, *J. Geophys. Res.*, *101*, 21,943–21,960, 1996.

Bennett, R. A., J. L. Davis, P. Elósegui, B. P. Wernicke, J. K. Snow, M. J. Abolins, M. A. House, G. L. Stirewalt, and D. A. Ferrill, Global Positioning System constraints on fault slip rates in the Death Valley region, California and Nevada, *Geophys. Res. Lett.*, *24*, 3073–3076, 1997.

Bennett, R. A., J. L. Davis, and B. P. Wernicke, Continuous GPS measurements of deformation across the northern basin and range province, *Geophys. Res. Lett.*, *25*, 563–566, 1998.

Bennett, R. A., J. L. Davis, and B. P. Wernicke, Large scale pattern of western U. S. Cordillera deformation, *Geology*, *27*, 371–374, 1999.

Bennett, R. A., J. L. Davis, B. P. Wernicke, and J. E. Normandeau, Space geodetic measurements of plate boundary deformation in the western U.S. Cordillera, in *Plate Boundary Zones*, *Geodyn. Ser.*, vol. 30, edited by S. A. Stein and J. T. Freymueller, pp. 27–55, 2002.

Beutler, G., I. I. Mueller, and R. E. Neilan, The International GPS Service for Geodynamics: Development and start of official service on January 1, 1994, *Bull. Geod.*, *68*, 39–70, 1994.

Burchfiel, B. C., and J. H. Stewart, "Pull-apart" origin of the central segment of Death Valley, California, *Geol. Soc. Am. Bull.*, *77*, 439–442, 1966.

Burchfiel, B. C., K. V. Hodges, and L. H. Royden, Geology of Panamint Valley–Saline Valley pull-apart system, California: Palinspastic evidence for low-angle geometry of a Neogene range-bounding fault, *J. Geophys. Res.*, *91*, 10,422–10,426, 1987.

Butler, P. R., B. W. Troxel, and K. L. Verosub, Late Cenozoic styles of deformation along the southern Death Valley Fault zone, California, *Geol. Soc. Am. Bull.*, *100*, 402–410, 1988.

Caskey, S., P. Wesnousky, S. G. Zhang, and D. Slemmons, Surface faulting of the 1954 Fairview Peak (M(S), 7.2) and Dixie Valley (M(S) 6.8) earthquakes, central Nevada, *Bull. Seismol. Soc. Am.*, *86*, 761–787, 1996.

Crespi, M., and G. P.-F. Riguzzi, Strain tensor estimation by GPS observations: Software and applications, *Boll. Geod. Sci. Affini*, *3*, 261–280, 2000.

Davis, J. L., et al., Assessment of GPS velocity accuracy for the Basin and Range Geodetic Network (BARGEN), *Geophys. Res. Lett.*, *30*, in press, 2003.

DeMets, C., and T. Dixon, New kinematic models for Pacific–North America motion from 3 Ma to present, I, Evidence for steady motion and biases in the NUVEL-1A model, *Geophys. Res. Lett.*, *13*, 1921–1924, 1999.

Dixon, T. H., R. Stefano, J. Lee, and M. C. Reheis, Constraints on present-day Basin and Range deformation from space geodesy, *Tectonics*, *14*, 755–772, 1995.

Dixon, T., A. Mao, M. Bursik, M. Heflin, J. Langbein, R. Stein, and F. Webb, Continuous monitoring of surface deformation at Long Valley Caldera, California, with GPS, *J. Geophys. Res.*, *102*, 12,017–12,034, 1997.

Dixon, T. H., M. Miller, F. Farina, H. Wang, and D. Johnson, Present-day motion of the Sierra Nevada block and some tectonic implications for the basin and range province, North America Cordillera, *Teconics*, *1*, 19–24, 2000.

Dokka, R. K., and C. J. Travis, Late Cenozoic strike-slip faulting in the Mojave desert, California, *Tectonics*, *9*, 311–340, 1990.

Doser, D., and H. Kanamori, Depth of seismicity in the Imperial Valley region (1977–1983) and its relationship to heat flow, crustal structure, and the Oc-

tober 15, 1979, earthquake, *J. Geophys. Res.*, *91*, 675–688, 1986.

England, P., and D. P. McKenzie, A thin viscous sheet model for continental deformation, *Geophys. J. R. Astron. Soc.*, *70*, 295–321, 1982.

England, P., G. Houseman, and L. Sonder, Length scales for continental deformation in convergent, divergent, and strike-slip environments: Analytical and approximate solutions for a thin viscous sheet model, *J. Geophys. Res.*, *90*, 3551–3557, 1985.

Fialko, Y., and M. Simons, Evidence for on-going inflation of the Socorro magma body, New Mexico, from interferometric synthetic aperture radar imaging, *Geophys. Res. Lett.*, *28*, 3549–3552, 2001a.

Fialko, Y., and M. Simons, Deformation and seismicity in the Coso geothermal area, Inyo County, California: Observations and modeling using satellite radar interferometry, *J. Geophys. Res.*, *105*, 21,781–21,793, 2001b.

Flesch, L. M., W. E. Holt, A. J. Haines, and B. Shen-Tu, Dynamics of the Pacific–North American plate boundary in the western United States, *Science*, *287*, 834–836, 2000.

Freymueller, J. T., M. H. Murray, P. Segall, and D. Castillo, Kinematics of the Pacific–North America plate boundary zone, northern California, *J. Geophys. Res.*, *104*, 7419–7441, 1999.

Friedrich, A., et al., Comparison of geodetic and geologic data from the Wasatch region, Utah, and implications for the spectral character of Earth deformation at periods of ten to ten million years, *J. Geophys. Res.*, *108*, doi:10.1029/2001JB000682, in press, 2003.

Gan, W., J. L. Svarc, J. C. Savage, and W. H. Prescott, Strain accumulation across the eastern California shear zone at latitud 36°30′N, *J. Geophys. Res.*, *105*, 16,229–16,236, 2000.

Haines, A., and W. Holt, A procedure for obtaining the complete horizontal motions within zones of distributed deformation from the inversion of strain-rate data, *J. Geophys. Res.*, *98*, 12,057–12,082, 1993.

Hearn, E. H., and E. D. Humphreys, Kinematics of the southern Walker Lane Belt and motion of the sierra nevada block, California, *J. Geophys. Res.*, *103*, 27,033–27,049, 1998.

Herring, T. A., GLOBK: Global Kalman filter VLBI and GPS analysis program, technical report, Dept. Earth, Atmos., and Planet. Sci., Mass. Inst. of Technol., Cambridge, Mass., 1999.

Humphreys, E. D., Post-Laramide removal of the Farallon slab, western United States, *Geology*, *23*, 987–990, 1995.

Jones, C., J. Unruh, and L. J. Sonder, The role of gravitational potential energy in active deformation of the southwestern United States, *Nature*, *381*, 37–41, 1996.

King, R. W., and Y. Bock, Documentation for the MIT GPS analysis software: GAMIT, technical report, Dept. Earth, Atmos. and Planet. Sci., Mass. Inst. of Technol., Cambridge, Mass., 1999.

King, N. E., J. L. Svarc, E. Fogelman, W. K. Gross, K. W. Clark, G. D. Hamilton, C. H. Stiffler, and J. M. Sutton, Continuous GPS observations across the Hayward fault, California, 1991–1994, *J. Geophys. Res.*, *100*, 20,271–20,283, 1995.

Larsen, S., and R. Reilinger, Evidence for ongoing crustal deformation related to magmatic activity near Socorro, New Mexico, *J. Geophys. Res.*, *91*, 6283–6292, 1986.

Lee, J., J. Spencer, and L. Owens, Holocene slip rates along the Owens Valley Fault, California: Implications for the recent evolution of the Eastern California Shear Zone, *Geology*, *29*, 819–822, 2001.

Lowry, A. R., and R. B. Smith, Strength and rheology of the western U.S. Cordillera, *J. Geophys. Res.*, *100*, 17,947–17,963, 1995.

Malservisi, R., K. Furlong, and T. Dixon, Influence of the earthquake cycle and lithospheric rheology on the dynamics of the eastern California shear zone, *Geophys. Res. Lett.*, *28*(14), doi:10.1029/2001GL013311, 2001.

McClusky, S., et al., Global Positioning System constraints on plate kinematics and dynamics in the eastern Mediterranean ad Caucasus, *J. Geophys. Res.*, *105*, 5659–5719, 2000.

McClusky, S., S. Bjornstad, B. Hager, R. King, B. Meade, M. Miller, F. Monastero, and B. Souter, Present day kinematics of the Eastern California Shear Zone from a geodetically constrained block model, *Geophys. Res. Lett.*, *28*, 3369–3372, 2001.

Miller, M., D. Johnson, T. Dixon, and R. Dokka, Refined kinematics of the eastern California shear zone from GPS observations, 1993–1998, *J. Geophys. Res.*, *106*, 2245–2263, 2001.

Minster, J. B., and T. H. Jordan, Vector constraints on western U.S. deformation from space geodesy, neotectonics and plate motions, *J. Geophys. Res.*, *92*, 4798–4804, 1987.

Molnar, P., Some simple physical aspects of the support, structure, and evolution of mountain belts, *Spec. Pap. Geol. Soc. Am.*, *218*, 179–207, 1988.

Molnar, P., and P. Tapponier, Cenozoic tectonics of Asia: Effects of a continental collision zone, *Science*, *189*, 419–426, 1975.

Morrison, R. B., Quaternary stratigraphic, hydrologic, and climatic history of the Great Basin, with emphasis on Lake Lahontan, Bonneville, and Tecopa, in *Quaternary Nonglacial Geology: Conterminous U.S.*, edited by R. B. Morrison, pp. 283–320, Geol. Soc. Am., Boulder, Colo., 1991.

Niemi, N. A., B. P. Wernicke, A. M. Friedrich, M. Simons, R. A. Bennett, and J. L. Davis, BARGEN continuous GPS data across the eastern Basin and Range province, and implications for fault system dynamics, *Geophys. J. Int.*, in press, 2003.

Oldow, J. S., G. Kohler, and R. Donelick, Late Cenozoic extensional transfer in the Walker Lane strike-slip belt, Nevada, *Geology*, *22*, 637–640, 1994.

Oldow, J., C. Aiken, J. Hare, J. Fergusono, and R. Hardyman, Active displacement transfer and differential block motion within the central Walker Lane, western great Basin, *Geology*, *29*, 19–22, 2001.

Parsons, T., G. A. Thompson, and N. H. Sleep, Mantle plume influence on the Neogene uplift and extension of the U S. western Cordillera?, *Geology*, *22*, 83–86, 1994.

Pezzopane, S. K., and R. J. Weldon II, Tectonic role of faulting in central Nevada, *Tectonics*, *12*, 1140–1169, 1993.

Prescott, W., J. Savage, J. Svarc, and D. Manaker, Deformation across the Pacific–North America plate boundary near San Francisco, California, *J. Geophys. Res.*, *106*, 6673–6682, 2001.

Reheis, M. C., and T. H. Dixon, Kinematics of the eastern California shear zone: Evidence for slip transfer from Owens and Saline Valley fault zones to Fish Lake Valley fault zone, *Geology*, *24*, 339–342, 1996.

Reheis, M. C., and T. L. Sawyer, Late Cenozoic history and slip rates of the Fish Lake Valley, Emigrant Peak, and Deep Springs fault zones, Nevada and California, *Geol. Soc. Am. Bull.*, *109*, 280–299, 1997.

Sauber, J., W. Thatcher, S. Solomon, and M. Lisowski, Geodetic slip rate for the eastern California shear zone and the recurrence time of Mojave desert earthquakes, *Nature*, *367*, 264–266, 1994.

Savage, J. C., and M. Lisowski, Strain accumulation in Owens Valley, California, *Bull. Seismol. Soc. Am.*, *85*, 151–158, 1995.

Savage, J., M. Lisowski, W. Prescott, and A. Sanford, Geodetic evidence of horizontal deformation across the Rio Grande rift near Socorro, New Mexico, *J. Geophys. Res.*, *85*, 7215–7220, 1980.

Savage, J. C., M. Lisowski, and W. Prescott, An apparent shear zone trending north-northwest across the Mojave Desert into Owens Valley, eastern California, *Geophys. Res. Lett.*, *17*, 2113–2116, 1990.

Savage, J. C., M. Lisowski, J. L. Svarc, and K. K. Gross, Strain accumulation across the central Nevada seismic zone, *J. Geophys. Res.*, *100*, 20,257–20,269, 1995.

Savage, J. C., J. Svrac, and W. Prescott, Strain accumulation at Yucca Mountain, Nevada, *J. Geophys. Res.*, *104*, 17,627–17,631, 1999.

Savage, J., J. Svarc, W. Prescott, and M. Murray, Deformation across the forearc of the Cascadia subduction zone at Cape Blanco, Oregon, *J. Geophys. Res.*, *105*, 3095–3102, 2000.

Shen-Tu, B., W. E. Holt, and A. J. Haines, The contemporary kinematics of the western United States determined from earthquake moment tensors, very long baseline interferometry, and GPS observations, *J. Geophys. Res.*, *103*, 18,807–18,118, 1998.

Sieh, K., et al., Near-field investigations of the Landers earthquake sequence, April to July 1992, *Science*, *260*, 171–176, 1993.

Smith, R. B., Intraplate tectonics of the western North American plate, *Tectophysics*, *37*, 323–336, 1977.

Smith, R., and M. Sbar, Contemporary tectonics and seismicity of western United-States with emphasis on intermountain seismic belt, *Geol. Soc. Am. Bull.*, *85*, 1205–1218, 1974.

Sonder, L. J., and C. H. Jones, Western United States extension: How the west was widened, *Annu. Rev. Earth Planet. Sci.*, *27*, 417–462, 1999.

Steiner, M. B., and S. G. Lucas, Paleomagnetism of the Late Triassic Petrified Forest Formation, Chinle Group, western United States: Further evidence of "large" rotation of the Colorado Plateau, *J. Geophys. Res.*, *105*, 25,791–25,808, 2000.

Stewart, J. H., Basin ad Range structure: A system of horsts and grabens produced by deep-seated extension, *Geol. Soc. Am. Bull.*, *82*, 1019–1044, 1971.

Stewart, J. H., Tectonics and the Walker Lane Belt, western Great Basin: Mesozoic and Cenozoic deformation in a zone of shear, in *Metamorphism and Crustal Evolution of the Western United States*, *Rubey*, vol. VII, edited by W. G. Ernst, pp. 683–713, Prentice-Hall, Old Tappan, N. J., 1988.

Thatcher, W., Microplate versus continuum descriptions of active tectonic deformation, *J. Geophys. Res.*, *100*, 3885–3894, 1995.

Thatcher, W., G. R. Foulger, B. R. Julian, J. Svarc, E. Quilty, and G. W. Bawden, Present-day deformation across the Basin and Range province, western United States, *Science*, *283*, 1714–1718, 1999.

Thompson, G., and D. Burke, Regional geophysics of the Basin and Range province, *Annu. Rev. Earth Planet. Sci.*, *2*, 213–238, 1974.

Unruh, J. R., and W. R. Lettis, Kinematics of transpressional deformation in the eastern San Francisco Bay region, California, *Geology*, *26*, 19–22, 1998.

Wallace, R. E., Patterns and timing of late Quaternary faulting in the Great Basin province and relation to some regional tectonic features, *J. Geophys. Res.*, *89*, 5763–5769, 1984a.

Wallace, R. E., Fault scarps formed during the earthquakes of October 2, 1915, in Pleasant Valley, Nevada, and some tectonic implications, *U.S. Geol. Serv. Prof. Paper*, *1274-A,B*, A1–A33, 1984b.

Wells, R., C. Weaver, and R. Blakely, Fore-arc migration in Cascadia and its neotectonic significance, *Geology*, *26*, 759–762, 1998.

Wernicke, B. P., Cenozoic extensional tectonics of the Cordillera, U.S., in *The Geology of North America*, vol. 63, *The Cordilleran Orogen: Conterminous*

U.S., edited by B. Burchfiet, P. Lipman, and M. Zoback, pp. 553–581, Geol. Soc. of Am., Boulder, Colo., 1992.

Wernicke, B., G. J. Axen, and J. K. Snow, Basin and Range extensional tectonics at the latitude of Las Vegas, Nevada, *Geol. Soc. Am. Bull.*, *100*, 1738–1757, 1988.

Wernicke, B. P., J. L. Davis, R. A. Bennett, P. Elósegui, M. J. Abolins, R. A. Brady, M. A. House, A. N. Niemi, and J. K. Snow, Anomalous strain accumulation in the Yucca Mountain area, Nevada, *Science*, *279*, 2096–2100, 1998.

Wernicke, B. P., A. M. Friedrich, N. A. Niemi, R. A. Bennett, and J. L. Davis, Dynamics of plate boundary fault systems from Basin and Range Geodetic Network (BARGEN) and geologic data, *GSA Today*, *10*, 1–3, 2000.

Wicks, C., W. Thatcher, F. Monastero, and M. Hasting, Steady state deformation of the Coso Range, east central California, inferred from satellite radar interferometry, *J. Geophys. Res.*, *106*, 13,769–13,780, 2001.

Wright, L., Late Cenozoic fault patterns and stress fields in the Great Basin and westward displacement of the Sierra Nevada block, *Geology*, *4*, 489–494, 1976.

Zhang, P. M., D. Ellis, D. Slemmons, and F. Mao, Right-lateral displacements and Holocene rate associated with prehistoric earthquakes along the southern Panamint Valley fault zone, *J. Geophys. Res.*, *95*, 4857–4872, 1990.

Zumberge, J., M. Hoflin, D. Jefferson, M. Watkins, and F. Webb, Precise point positioning for the efficient and robust analysis of GPS data from large networks, *J. Geophys. Res.*, *102*, 5005–5017, 1997.

R. A. Bennett and J. L. Davis, Harvard-Smithsonian Center for Astrophysics, 60 Garden Street, MS 42, Cambridge, MA 02138-1516, USA. (rbennett@cfa.Harvard.edu)

A. Friedrich, Institut für Geowissenschaften, Universität Potsdam, Karl-Liebknechtstr. 24/H25, 14476, Golm, Germany.

N. Niemi, Department of Geological Sciences, UC Santa Barbara, Building 526, Santa Barbara, CA 93106-9630, USA.

B. Wernicke, Division of Geological and Planetary Sciences, California Institute of Technology, 1200 East California Blvd., Pasadena, CA 91125, USA.